RESEARCH ARTICLE

ADVANCED MATERIALS

www.advmat.de

Engineering Pore Environments of Sulfate-Pillared Metal-Organic Framework for Efficient C_2H_2/CO_2 Separation with Record Selectivity

*Xing Liu, Peixin Zhang, Hanting Xiong, Yan Zhang, Ke Wu, Junhui Liu, Rajamani Krishna, Jingwen Chen, Shixia Chen, Zheling Zeng, Shuguang Deng, and Jun Wang**

Engineering pore environments exhibit great potential in improving gas adsorption and separation performances but require specific means for acetylene/carbon dioxide (C_2H_2/CO_2) separation due to their identical dynamic diameters and similar properties. Herein, a novel sulfate-pillared MOF adsorbent (SOFOUR-TEPE-Zn) using 1,1,2,2-tetra(pyridin-4-yl) ethene (TEPE) ligand with dense electronegative pore surfaces is reported. Compared to the prototype SOFOUR-1-Zn, SOFOUR-TEPE-Zn exhibits a higher C_2H_2 uptake (89.1 $cm^3\ g^{-1}$), meanwhile the CO_2 uptake reduces to 14.1 $cm^3\ g^{-1}$, only 17.4% of that on SOFOUR-1-Zn (81.0 $cm^3\ g^{-1}$). The high affinity toward C_2H_2 than CO_2 is demonstrated by the benchmark C_2H_2/CO_2 selectivity (16 833). Furthermore, dynamic breakthrough experiments confirm its application feasibility and good cyclability at various flow rates. During the desorption cycle, 60.1 $cm^3\ g^{-1}$ C_2H_2 of 99.5% purity or 33.2 $cm^3\ g^{-1}$ C_2H_2 of 99.99% purity can be recovered by stepped purging and mild heating. The simulated pressure swing adsorption processes reveal that 75.5 $cm^3\ g^{-1}$ C_2H_2 of 99.5+% purity with a high gas recovery of 99.82% can be produced in a counter-current blowdown process. Modeling studies disclose four favorable adsorption sites and dense packing for C_2H_2.

1. Introduction

High-purity acetylene (>99%) is an essential raw material for manufacturing chemical commodities such as vinyl and acrylate polymers.[1] In industry, acetylene (C_2H_2) is commonly produced by partial combustion of methane or thermal cracking of hydrocarbons, wherein carbon dioxide (CO_2) unavoidably coexists and impairs the subsequent utilization efficiency.[2] The separation of C_2H_2 from C_2H_2/CO_2 gas-mixtures prevailingly relies on cryogenic distillations associating high energy input owing to their close boiling points (189.3 K for C_2H_2 and 194.7 K for CO_2).[3,4] In contrast, adsorption technology employing porous adsorbents emerges as a promising alternative for light hydrocarbon separations that can operate at ambient conditions achieving high energy efficiency.[4,5] Nevertheless, adsorptive separation of C_2H_2/CO_2 gas-mixture is recognized as one of the most challenging systems because of their identical kinetic molecular sizes (3.3 Å) and similar molecular polarizability (33.3×10^{25} cm^3 for C_2H_2 and 29.1×10^{25} cm^3 for CO_2).[6] Over the last decade, metal-organic frameworks (MOFs) have shown considerable progress in hydrocarbon separations due to their structural designability and tunability on pore size/shape and functionality.[7–10] Exposing open metal sites (OMSs) is the general approach to recognizing C_2H_2 over CO_2 and thus achieving improved C_2H_2/CO_2 separation performances, as demonstrated in ZJU-74a,[11] MOF-74,[12] ATC-Cu,[13] and NKMOF-1-Ni.[14] Although relatively large C_2H_2 uptakes can be obtained in this type of MOFs, enhanced CO_2 adsorptions concurrently occur due to electrostatic interactions, generating moderate C_2H_2/CO_2 selectivity.[15] For example, the highest C_2H_2/CO_2 selectivity of 185.0 on MOFs with OMSs was reported on Cu^I@UiO-66-$(COOH)_2$.[16] Recently, several flexible MOFs have realized significantly high C_2H_2/CO_2 selectivity exploiting the differences in guest-host interactions and gate-open pressures.[17–19] But, in fixed adsorption columns, the possible co-adsorption will generate low-purity C_2H_2 product in the recovery process.[20]

X. Liu, P. Zhang, H. Xiong, Y. Zhang, K. Wu, J. Liu, J. Chen, S. Chen, Z. Zeng, J. Wang
Chemistry and Chemical Engineering School
Nanchang University
Nanchang, Jiangxi 330031, China
E-mail: jwang7@ncu.edu.cn

R. Krishna
Van't Hoff Institute for Molecular Sciences
University of Amsterdam
Science Park 904, Amsterdam 1098 XH, Netherlands

S. Deng
School for Engineering of Matter
Transport and Energy
Arizona State University
Tempe, AZ 85287, USA

The ORCID identification number(s) for the author(s) of this article can be found under https://doi.org/10.1002/adma.202210415.

DOI: 10.1002/adma.202210415

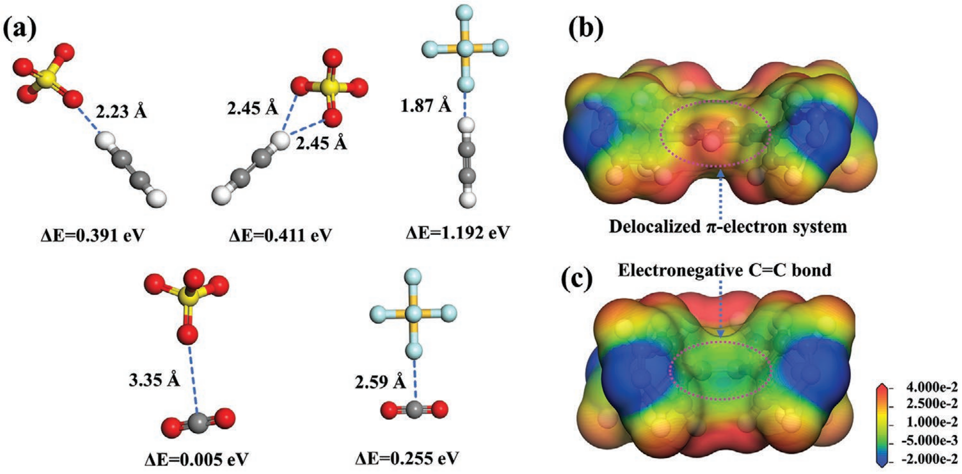

Figure 1. a) DFT calculated adsorption energies for C_2H_2 and CO_2 on SO_4^{2-} and SiF_6^{2-} anions. The molecular electrostatic potential (MESP) mapping for b) TEPB and c) TEPE organic ligands.

Given the opposite electrostatic potentials of C_2H_2 and CO_2 molecules (Figure S2, Supporting Information), constructing negative pore environments forms electrostatic interactions to the π-electrons and hydrogen bonding to the acidic and positively-charged H atoms on C_2H_2.[21] Meanwhile, the electro-induced repulsion impedes the entrance of CO_2 with negatively-charged ends.[22] By incorporating electronegative hydrogen-bonding acceptors such as open oxygen and fluoride sites, some MOF adsorbents showed enhanced C_2H_2 capacity but with high adsorption enthalpy over 50 kJ mol^{-1}, making C_2H_2 recovery and adsorbent regeneration processes energy-intensive.[6,23] To solve this problem, less negatively-charged halogen and boron atoms were incorporated to further discriminate C_2H_2 over CO_2.[24,25] Compared to MOFs with fluorinated anions (SiF_6^{2-}, TiF_6^{2-}, GeF_6^{2-}, etc.), [Cu(TMBP)X] (TMBP = 3,3′,5,5′-tetramethyl-4,4′-bipyrazole; X = Cl, Br, I),[25] and ZNU-1 [$CuB_{12}H_{12}(dpe)_2$] (dpe = 1,2-di(4-pyridyl)ethylene)[24] exhibited moderate C_2H_2/CO_2 selectivity of 16.9 and 56.6, respectively. Recently, our group demonstrated a novel Hofmann-type MOF adsorbent with negatively-charged pore environments, [Cu(NP)(bpy)] (NP = nitroprusside, bpy = 4,4′-bipyridine), showing leading C_2H_2/CO_2 selectivity of 47.2 among rigid MOFs.[22] Note that tuning the charge distributions on pore surfaces can also reverse the adsorption precedence that favorably adsorbs CO_2 over C_2H_2.[26–28] Despite the power of this strategy, elaborated modification and adjustment of pore environments are necessitated for constructing efficient MOF adsorbents with high C_2H_2 capacity and C_2H_2/CO_2 selectivity.[29,30]

Zaworotko's group reported the first sulfate-pillared hybrid ultramicroporous material, SOFOUR-1-Zn, [$Zn(tepb)(SO_4^{2-})]_n$ (TEPB = tetra(4-pyridyl)benzene, Figure S3a, Supporting Information), which showed smaller pore sizes with periodically expanded and contracted apertures by implanting shorter tetrahedral SO_4^{2-} rather than hexahedral SiF_6^{2-} anions.[31] Unfortunately, SOFOUR-1-Zn exhibited a lower uptake for C_2H_2 (69.4 cm^3 g^{-1}) than CO_2 (81.0 cm^3 g^{-1}) at 1 bar, rendering a relatively low C_2H_2/CO_2 selectivity of 6.6. We further conducted density functional theory (DFT) calculations for adsorption energies of C_2H_2 and CO_2 on SO_4^{2-} and SiF_6^{2-} anions. As shown in **Figure 1**a, SO_4^{2-} anion could interact with C_2H_2 with two configurations but show lower binding energy than SiF_6^{2-} anion. It is worth noting that SO_4^{2-} anion displays negligible interaction for CO_2 with a binding energy of 0.005 eV compared to SiF_6^{2-} (0.255 eV). Although these results seem contradictory to the adsorption capacity of C_2H_2 and CO_2 on SOFOUR-1-Zn, further highlighting that judicious choice of organic ligands also determines C_2H_2/CO_2 separation performances by impacting electro-environments on pore surfaces.[32] The center benzene ring in TEPB ligand contains delocalized π-electron systems that can accept or donate electrons (Figure 1b and Figure S3a, Supporting Information), thus we speculate that replacing the benzene ring with higher electronegative moieties will significantly enhance C_2H_2 adsorption while remaining low CO_2 uptake in sulfate-pillared MOFs.

Herein, we report a novel sulfate-pillared MOF adsorbent using 1,1,2,2-tetra(pyridin-4-yl) ethene (TEPE) ligand with higher electronegative ethylene linkage (C=C, Figure 1c and Figure S3b, Supporting Information). As a result, the obtained SOFOUR-TEPE-Zn, [$Zn(TEPE)(SO_4^{2-})]_n$, shows more electron-rich pore surfaces than the prototype SOFOUR-1-Zn, rendering a higher C_2H_2 uptake (89.1 cm^3 g^{-1}) than that of SOFOUR-1-Zn (69.4 cm^3 g^{-1}). Noticeably, the CO_2 adsorption capacity significantly reduces to 14.1 cm^3 g^{-1} on SOFOUR-TEPE-Zn, which is only 17.4% to that of SOFOUR-1-Zn (81.0 cm^3 g^{-1}). The high affinity toward C_2H_2 than CO_2 is further demonstrated by the benchmark C_2H_2/CO_2 (50:50, v/v) selectivity (16833) at ambient conditions. Furthermore, dynamic breakthrough experiments with equimolar C_2H_2/CO_2 gas-mixtures confirm the application feasibility and good cyclability of SOFOUR-TEPE-Zn. During the desorption cycle, 60.1 cm^3 g^{-1} C_2H_2 of 99.5% purity or 33.2 cm^3 g^{-1} C_2H_2 of 99.99% purity can be recovered from a single adsorption column by stepped purging and mild heating. The simulated pressure swing adsorption (PSA) processes reveal that 75.5 cm^3 g^{-1} C_2H_2 of 99.5+% purity with a high recovery of 99.82% could be recovered in counter-current blowdown process. Modeling studies disclose four favorable adsorption sites for C_2H_2, which are missing for CO_2.

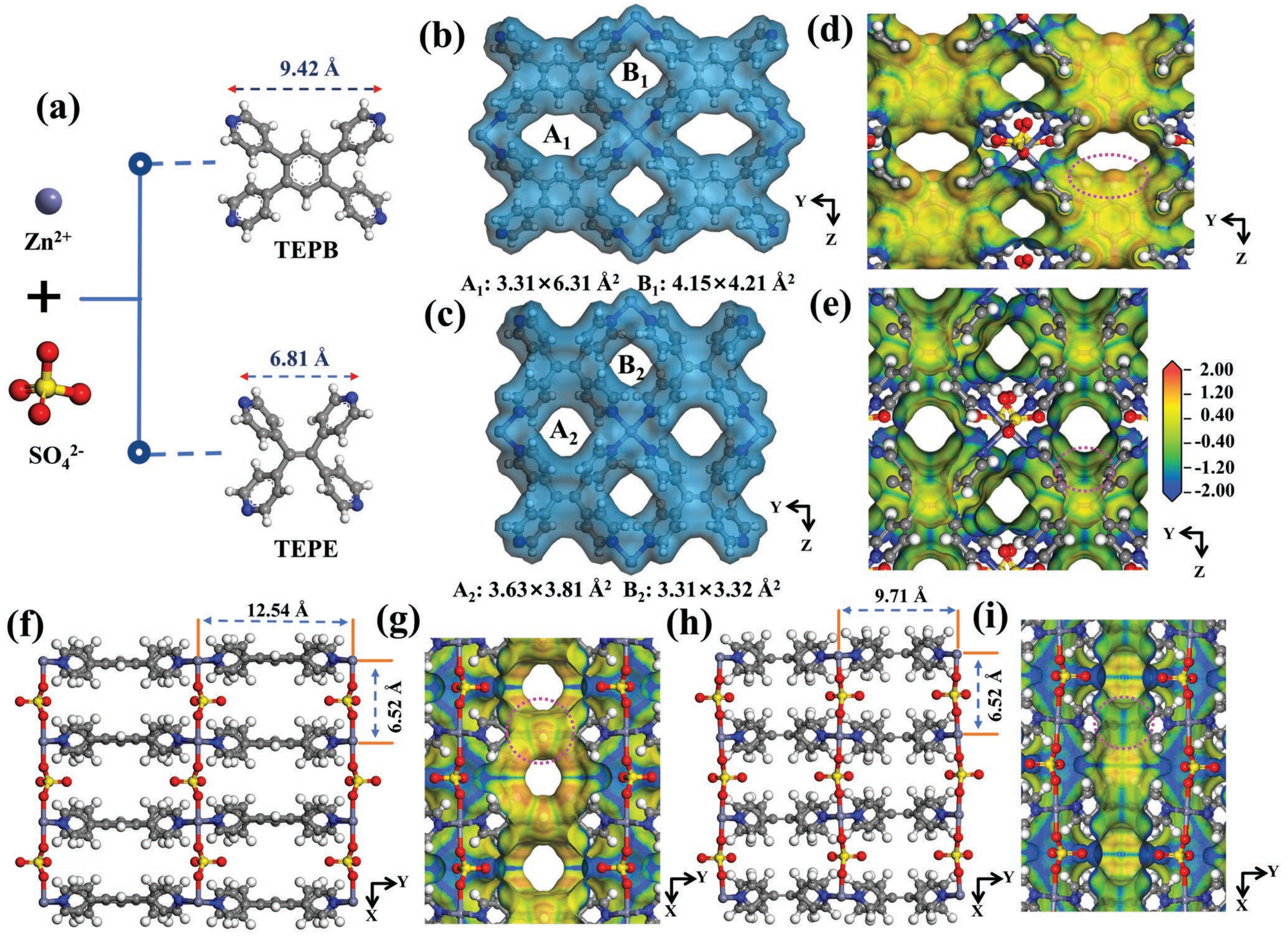

Figure 2. a) The building blocks of SOFOUR-1-Zn and SOFOUR-TEPE-Zn. Structure of SOFOUR-1-Zn viewed along the b) *X*-axes and f) *Z*-axes. Structure of SOFOUR-TEPE-Zn viewed along the c) *X*-axes and h) *Z*-axes. The Electrostatic surface potential of d,g) SOFOUR-1-Zn and e,i) SOFOUR-TEPE-Zn.

2. Results and Discussion

2.1. Sample Synthesis and Characterizations

The reaction of equal molar $ZnSO_4$ $7H_2O$ and TEPE at room temperature afforded microcrystalline powder of SOFOUR-TEPE-Zn (**Figure 2**a). Despite extensive attempts, it was not successful in obtaining high-quality single crystals for single-crystal X-ray diffraction studies. The structure of SOFOUR-TEPE-Zn was determined by Rietveld refinement of powder X-ray diffraction (PXRD) pattern (Figure S4 and Tables S1–S3, Supporting Information), which crystalized in the *Cmm2* space group, same as the prototype SOFOUR-1-Zn.[31] Structure analysis revealed that each Zn(II) atom was coordinated by four terminal nitrogen atoms of independent TEPE/TEPB ligands, generating 2D $[Zn (TEPB/TEPE)]_n$ layers (Figure 2b,c), which were further pillared by SO_4^{2-} anions to form 3D networks without interpenetration (Figure 2f,h). Owing to the smaller size of TEPE, the Zn−Zn distance reduced from 12.54 to 9.71 Å along the *Y*-axis. Consequently, the two distinct pores contracted from 3.31 × 6.31 and 4.15 × 4.21 Å^2 on SOFOUR-1-Zn to 3.63 × 3.81 and 3.31 × 3.32 Å^2 on SOFOUR-TEPE-Zn, respectively. The phase purity of bulk SOFOUR-TEPE-Zn was confirmed by comparing the as-synthesized sample with the simulated pattern, meanwhile, the unchanged PXRD pattern of the activated sample indicated the structural rigidity (Figure S5, Supporting Information). The simulated and experimental XRD patterns of SOFOUR-1-Zn were presented in Figure S6, Supporting Information. We further mapped the electrostatic surface potential distributions of the cavities by DFT calculations. After ligand substitution, the C=C moieties in SOFOUR-TEPE-Zn draw more electrons than the benzene ring in SOFOUR-1-Zn along the *X*-axis due to its higher electronegativity (Figure 2d,e). Meanwhile, along the *Z*-axis, the negatively-charged C atoms of ethylene linkages were unmasked (Figure 2i), in contrast to the exposed positively-charged H atoms of benzene rings (Figure 2g). Therefore, the interlayer spaces sandwiched by organic ligands also showed electronegative pore surfaces. Combined with the smaller pore sizes, a much denser electronegative pore environment was successfully constructed in SOFOUR-TEPE-Zn.

To further confirm the purity of as-synthesized SOFOUR-TEPE-Zn, ^{1}H nuclear magnetic resonance spectroscopy (NMR) and ^{13}C NMR spectra of digested SOFOUR-TEPE-Zn exhibited identical characteristic peaks of carbon and hydrogen with TEPE ligand (Figures S7 and S8, Supporting Information). The ultimate elemental analysis showed that the content of each element matched well the theoretical formula of SOFOUR-TEPE-Zn ($C_{22}H_{16}N_4O_4SZn$, Table S4, Supporting Information). The characteristic content ratio of N/S in as-synthesized SOFOUR-TEPE-Zn (1.69) was also close to the theoretical value (1.75). The scanning electron microscopy (SEM) image showed the uniform thin-plate morphology of SOFOUR-TEPE-Zn with a thickness of 50–60 nm. (Figure S9, Supporting Information), consistent with the results of transmission electron microscopy (Figure S10, Supporting Information). The energy dispersive X-ray spectroscopy (EDX) demonstrated the even distributions of C, N, O, S, and Zn elements (Figure S11, Supporting Information), which was further confirmed by the X-ray photoelectron spectroscopy (Figure S12, Supporting Information). Fourier transform infrared spectroscopy (FT-IR) spectra showed the characteristic peaks of stretching vibrations of S=O in SO_4^{2-} pillars at 1116.6 and 1071.0 cm^{-1} and Zn-O stretching vibrations at 589.3 and 469.3 cm^{-1} (Figure S13, Supporting Information). The permanent porosity was probed by CO_2 adsorption at 195 K (Figure S14, Supporting Information), SOFOUR-TEPE-Zn showed a smaller Brunauer–Emmett–Teller (BET) specific surface area of 410.96 $m^2 g^{-1}$ than SOFOUR-1-Zn (612.1 $m^2 g^{-1}$) with a total pore volume of 0.14 $cm^3 g^{-1}$. The negligible N_2 adsorption at 77 K and Ar adsorption at 87 K confirmed its ultramicroporous nature (Figure S15, Supporting Information). The structural stability was examined by immersing SOFOUR-TEPE-Zn in various organic solvents for 10 days and boiling water for 72 h, intact PXRD patterns were maintained (Figure S16, Supporting Information). Thermogravimetric analysis disclosed that the thermal stability of SOFOUR-TEPE-Zn reached ca. 330 °C (Figure S17, Supporting Information).

2.2. Adsorption and Separation Performances

Considering the unique pore chemistry and suitable aperture sizes, single-component C_2H_2 and CO_2 equilibrium sorption isotherms were collected, and notable differences in adsorption capacities were observed (**Figure 3**a). SOFOUR-TEPE-Zn exhibited steep C_2H_2 adsorption in low-pressure regions and reached a total C_2H_2 uptake of 89.1 $cm^3 g^{-1}$ at 298 K and 1.0 bar, higher than that of SOFOUR-1-Zn (69.4 $cm^3 g^{-1}$). Intriguingly, the CO_2 adsorption capacity significantly decreased to 14.1 $cm^3 g^{-1}$ on SOFOUR-TEPE-Zn, which was only 17.4% of that on SOFOUR-1-Zn (81.0 $cm^3 g^{-1}$). The adsorption results implied potent C_2H_2/CO_2 separation performances, therein the C_2H_2 uptake at practical partial pressure (0.5 bar) should also be concerned. In this regard, the C_2H_2 adsorption capacity was measured to be 82.7 $cm^3 g^{-1}$ at 0.5 bar and 298 K on SOFOUR-TEPE-Zn (Figure 3d), outperforming that of many top-ranking adsorbents, including NKMOF-1-Ni (55.5 $cm^3 g^{-1}$),[14] ZNU-1 (70.0 $cm^3 g^{-1}$),[24] CAU-10-NH_2 (76.3 $cm^3 g^{-1}$),[33] FJU-6-TATB (73.0 $cm^3 g^{-1}$),[34] and Cu@UiO-66-$(COOH)_2$ (43.4 $cm^3 g^{-1}$).[16] Furthermore, adsorption kinetics should be particularly emphasized in adsorptive processes, the time-dependent gas uptake profiles of C_2H_2 and CO_2 were recorded (Figure 3b). The adsorption kinetic curves disclosed that C_2H_2 and CO_2 reached the equilibrium at almost the same time (≈4.1 min), but the

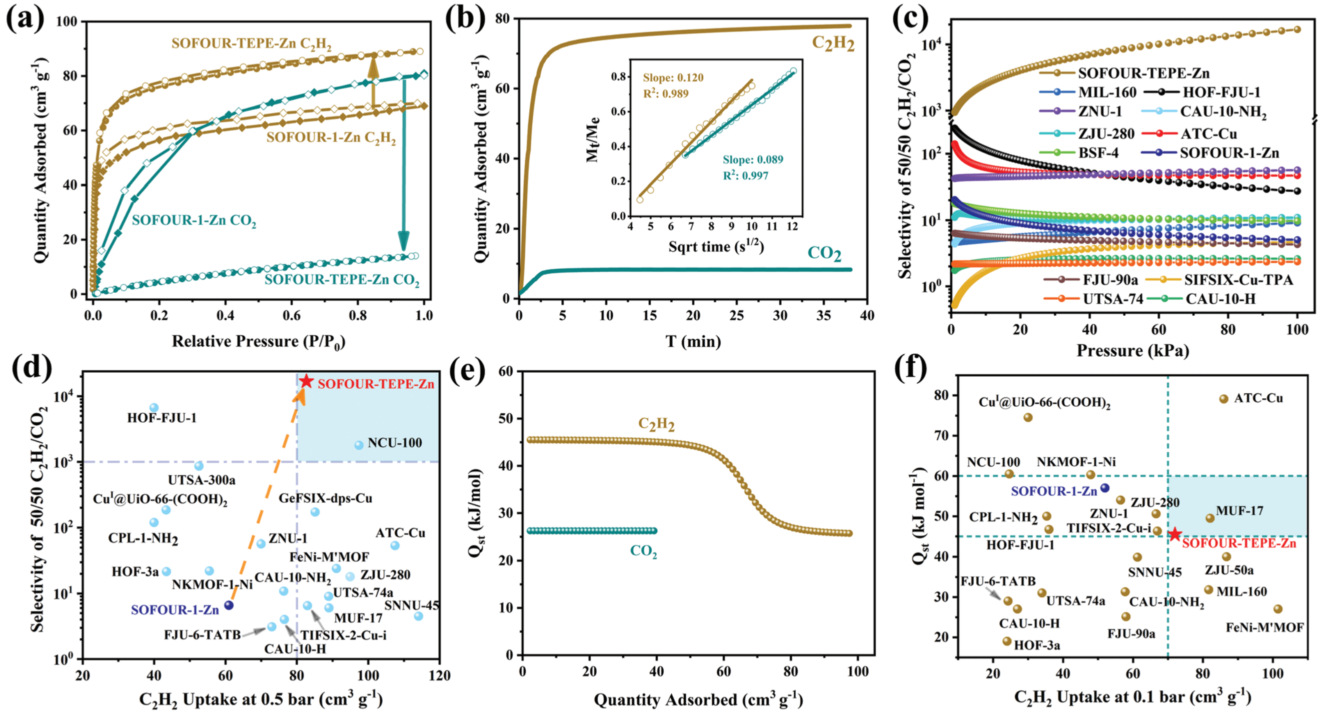

Figure 3. a) C_2H_2 and CO_2 adsorption isotherms for SOFOUR-1-Zn and SOFOUR-TEPE-Zn at 298 K. b) Kinetic adsorption profiles of SOFOUR-TEPE-Zn for C_2H_2 and CO_2 at an equilibrium pressure of 500 mbar (Pressure rise rate: 200 mbar min^{-1}, 298 K). c) IAST adsorption selectivity curves and comparison of SOFOUR-TEPE-Zn for a 50:50 C_2H_2/CO_2 mixture at 298 K. d) Comparison of C_2H_2 uptake at 0.5 bar versus C_2H_2/CO_2 selectivity and e) Q_{st} of C_2H_2 and CO_2 for SOFOUR-TEPE-Zn. f) Comparison plot for Q_{st} of C_2H_2 and C_2H_2 uptake at 0.1 bar and 298 K.

difference in adsorption capacities was also apparent (77.9 cm^3 g^{-1} for C_2H_2 vs 8.3 cm^3 g^{-1} for CO_2). The diffusional time constant (D', D/r^2) of C_2H_2 and CO_2 was calculated to be 1.3×10^{-3} s^{-1} and 6.9×10^{-4} s^{-1}, respectively. The low C_2H_2/CO_2 kinetic separation selectivity of 1.9 indicated its negligible kinetic separation performances.

To assess the separation potential of SOFOUR-TEPE-Zn for C_2H_2/CO_2 gas-mixtures, ideal adsorbed solution theory (IAST) was applied to quantitatively evaluate the separation selectivity. The dual-site Langmuir (DSL) model fitted the adsorption isotherms with excellent accuracy (Table S5, Supporting Information). SOFOUR-TEPE-Zn showed a record-high IAST C_2H_2/CO_2 (50:50, v/v) selectivity of 16 833 at 298 K (Figure 3c), 2250-times higher than SOFOUR-1-Zn (6.6)[31] and surpassing other best-performing adsorbents such as ZNU-1(56.6),[24] CPL-1-NH$_2$ (119),[35] ATC-Cu (53.6),[13] Cu@Uio-66-(COOH)$_2$ (73.9),[16] FJU-HOF-1 (6675.0 at 323 K),[21] UTSA-300a (860.0),[17] and NCU-100a (1786.6).[36] The record separation selectivity accompanied with high C_2H_2 uptake at 0.5 bar suggested SOFOUR-TEPE-Zn as a new benchmark adsorbent for C_2H_2/CO_2 separation (Figure 3d). Moreover, the maximum amount of C_2H_2 that can be recovered from C_2H_2/CO_2 gas-mixture represented by the separation potentials (Δq_{IAST}) was calculated.[37,38] SOFOUR-TEPE-Zn exhibited a superior Δq_{IAST} of 82.7 cm^3 g^{-1} (Figure S19, Supporting Information), almost double the value on SOFOUR-1-Zn (44.6 cm^3 g^{-1}) and higher than most C_2H_2/CO_2 adsorbents such as ZJU-280 (79.4 cm^3 g^{-1}), CAU-10-NH$_2$ (75.9 cm^3 g^{-1}), ZNU-1 (67.9 cm^3 g^{-1}), HOF-FJU-1 (39.9 cm^3 g^{-1}), and BSF-4 (37.9 cm^3 g^{-1}, Figures S21–S31, Supporting Information).

The isosteric heat of adsorption (Q_{st}) was calculated to evaluate the binding affinity between adsorbent and adsorbates. The Q_{st} of C_2H_2 at near-zero loading of 45.6 kJ mol^{-1} belonged to the "sweet spot" region (45–60 kJ mol^{-1}) that allows both firm binding and energy-efficient regeneration (Figure 3e).[31,39] The ten consecutive cycles of C_2H_2 and CO_2 adsorptions verified the facile and complete reversible adsorption behaviors on SOFOUR-TEPE-Zn (Figure S20, Supporting Information). In contrast, the Q_{st} of CO_2 was calculated to be 26.3 kJ mol^{-1}, such distinct Q_{st} values supported the preferential C_2H_2 adsorption and high C_2H_2/CO_2 selectivity. The steep C_2H_2 uptake at low-pressure ranges on SOFOUR-TEPE-Zn also evidenced the strong C_2H_2 affinity.[13] On the other hand, the C_2H_2 yields of different industrial production routes are variable, for instance, high-temperature plasma pyrolysis of CH_4 yields 80–90% C_2H_2 and 10–20% CO_2.[40,41] As expected, SOFOUR-TEPE-Zn exhibited a high C_2H_2 uptake of 72.01 cm^3 g^{-1} at 0.1 bar and 298 K, surpassing most C_2H_2 adsorbents such as SOFOUR-1-Zn (52.0 cm^3 g^{-1}), NKMOF-1-Ni (48.0 cm^3 g^{-1}),[14] CPL-1-NH$_2$ (35.4 cm^3 g^{-1}),[35] ZNU-1 (56.4 cm^3 g^{-1}),[24] FJU-90a (58.0 cm^3 g^{-1}),[42] and SNNU-45 (61.3 cm^3 g^{-1}).[43] Note that SOFOUR-TEPE-Zn was one of two exceptional adsorbents showing suitable Q_{st} of C_2H_2 and high C_2H_2 uptake (>70 cm^3 g^{-1}, Figure 3f).

2.3. Modeling Simulation Studies

To gain precise insights into the binding sites of C_2H_2 and CO_2 in SOFOUR-TEPE-Zn, modeling studies using first-principles dispersion-corrected density functional theory (DFT-D) and grand canonical Monte Carlo (GCMC) simulations were carried out. The dense C_2H_2 packing pattern showed four distinct adsorption sites in SOFOUR-TEPE-Zn (**Figure 4**a and Figure S32, Supporting Information). In Site-I, C_2H_2 was firmly captured by the O atom of SO_4^{2-} pillar through C—H···O bond with a distance of 2.18 Å. Besides, four H—C···H bonds were formed between C_2H_2 and neighboring pyridine rings showing distances of 2.90–2.96 Å (Figure 4b). In Site-II and Site-III, similar binding patterns existed as three C—H···O bonds with distances of 2.04–2.78 Å and two H—C···H bonds with distances of 2.61–2.64 Å (Figure 4c,d). Whereas the C_2H_2 was cooperatively interacted by four H—C···H bonds in Site-IV with distances of 3.01–3.33 Å (Figure 4e). Meanwhile, due to the dense distributions of C_2H_2, guest-guest interactions were also observed in pore channels (Figure S33a, Supporting Information). For the C_2H_2 packing pattern in SOFOUR-1-Zn, the distances of C—H···O (2.02–2.63 Å) and H—C···H (2.55–3.70 Å) bonds between C_2H_2 and SOFOUR-1-Zn were relatively longer than that in SOFOUR-TEPE-Zn (Figures S34 and S35, Supporting Information), indicating the weaker C_2H_2 capture capability. In sharp contrast, the CO_2 molecule could only form weak O—C···H van der Waals (vdW) interactions (2.71–2.93 Å) with the H atoms of the pyridine rings of SOFOUR-TEPE-Zn (Figure S36, Supporting Information). Note that no evidence for interactions between CO_2 and SO_4^{2-} pillar in SOFOUR-TEPE-Zn, and no efficient CO_2 packing was observed due to the electro-repulsive effect (Figure S36, Supporting Information). Whereas, strong interactions were observed between CO_2 and SO_4^{2-} pillar via O—C···O—S bonds (2.80 and 2.86 Å) and SOFOUR-1-Zn framework via O—C···H bonds (2.45–3.64 Å, Figures S37 and S38, Supporting Information). The low-loading adsorption enthalpy of C_2H_2 with SOFOUR-TEPE-Zn was calculated to be −54.7, −71.2, −63.0, and −45.7 kJ mol^{-1} in Site-I, Site-II, Site-III, and Site-IV respectively. Furthermore, the distribution density of C_2H_2 was illustrated by GCMC simulations. At 1 kPa, the adsorbed C_2H_2 molecules were distributed near DFT-derived adsorption sites (Figure S39, Supporting Information). As the loading-pressure increased to 50 kPa, no new adsorption location emerged, and the C_2H_2 distribution density enhanced (Figure S40, Supporting Information). Intriguing, the C_2H_2 distribution density merely changed at 100 kPa (Figure S41, Supporting Information), suggesting the rapid C_2H_2 adsorption and saturation before 50 kPa.

The charge transfer analysis on the gas-loaded structures was further performed, in which the blue and yellow surfaces indicate charge accumulation and depletion, respectively. At Sites I-III, strong potential-field induced electron bias was generated between H atoms of C_2H_2 and O atoms of SO_4^{2-} pillars (Figure 4f and Figure S33b, Supporting Information). Notably, the originally positively-charged H atoms of C_2H_2 were almost entirely surrounded by negative electrons, and a large proportion of positrons were clustered around the O atoms of SO_4^{2-} pillars. The apparent guest-host charge transfers demonstrated that the electron-potential derived mechanisms endowed strong C_2H_2 adsorptions in SOFOUR-TEPE-Zn. Comparably, at Site-IV, relatively weak guest-host charge transfers between H atoms of C_2H_2 and C=C bonds occurred (Figure S42, Supporting Information). On the contrary, the charge transfer between CO_2 molecule and SOFOUR-TEPE-Zn framework

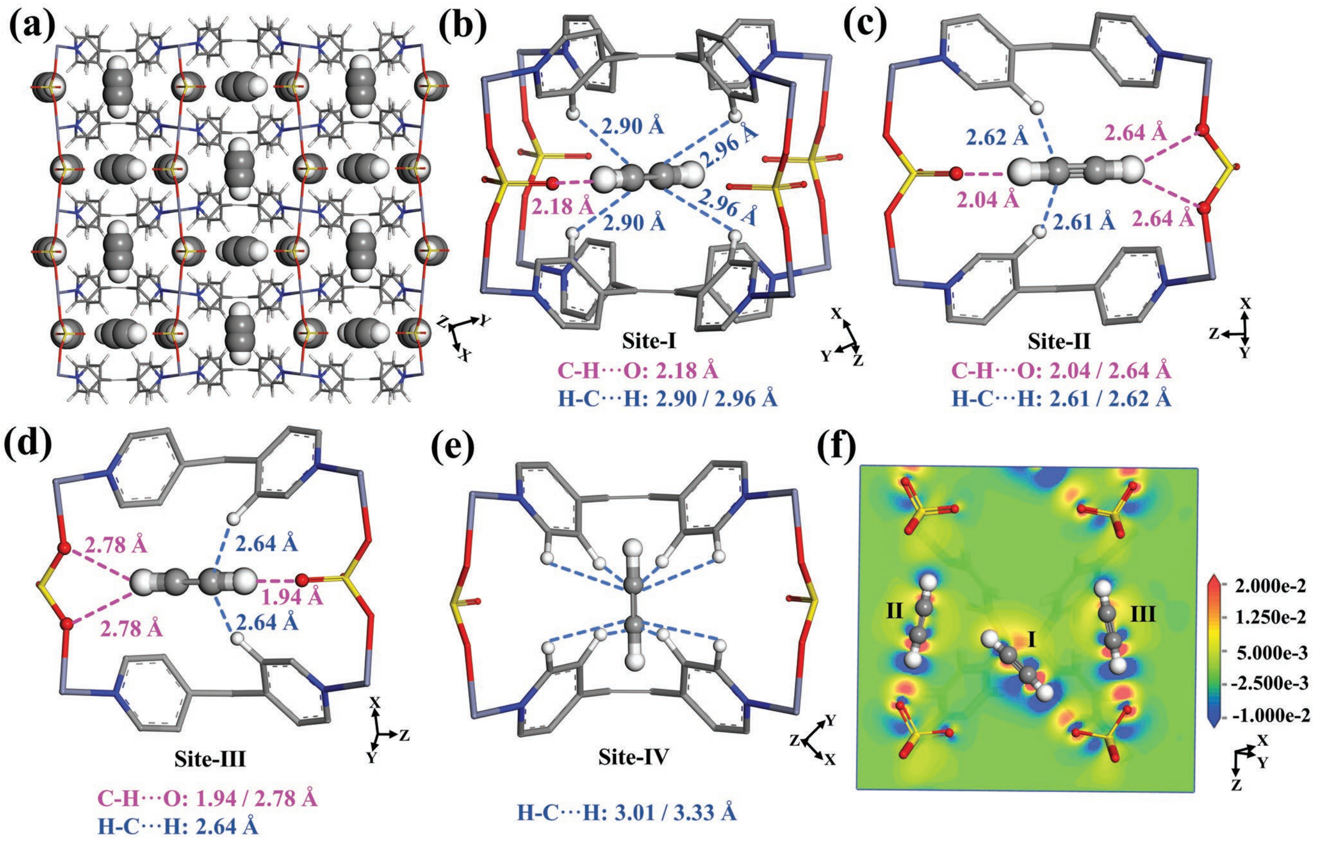

Figure 4. a) Dense packing of C_2H_2 molecules in SOFOUR-TEPE-Zn viewed along the *Z*-axes. b–e) C_2H_2 binding sites in SOFOUR-TEPE-Zn by theoretical studies. f) Charge density difference plots of C_2H_2-loaded structure.

was negligible (Figure S43, Supporting Information). However, both C_2H_2 and CO_2 molecules generated strong potential-field-induced electron bias with SOFOUR-1-Zn (Figures S44 and S45, Supporting Information). Therefore, the dense negative electrostatic potential environments constructed by SO_4^{2-} pillars and TEPE ligand-induced the preferred C_2H_2 binding over CO_2 on SOFOUR-TEPE-Zn.

2.4. Transient Breakthrough Experiments and PSA Simulations

To demonstrate the feasibility in industrial processes of using SOFOUR-TEPE-Zn under dynamic conditions, transient breakthrough experiments at three different flow rates were carried out for binary C_2H_2/CO_2 (50/50, v/v) mixtures at room temperature (**Figure 5**a). Clean C_2H_2/CO_2 separations were obtained at three flow rates, and the simulated breakthrough curves matched well with the experimental ones (Figures S48–S50, Supporting Information). With the binary gas-mixture injected into the adsorption bed at the flow rate of 2.0 mL min^{-1}, the CO_2 passed through the bed quickly at ≈4.2 min g^{-1}, whereas the C_2H_2 was retained for 63.3 min g^{-1}. When the flow rates increased to 5.0 and 10.0 mL min^{-1}, the breakthrough point for C_2H_2 decreased to 25.4 and 12.3 min g^{-1}, and the clean separations were still retained. The corresponding dynamic C_2H_2 adsorption amount was calculated to be 72.0, 70.8, and 68.1 cm^3 g^{-1} at 2.0, 5.0, and 10.0 mL min^{-1}, respectively. More importantly, high-purity C_2H_2 product was generated during desorption processes, thus the desorption conditions and methods should be investigated but commonly less explored. In this work, we applied a two-step desorption process to collect as many high-purity C_2H_2 products as possible. The saturated adsorption column was purged by helium (He) stream at 10.0 mL min^{-1} and 298 K to blow out weakly adsorbed C_2H_2, then heated to 343 K to extract firmly adsorbed C_2H_2. As illustrated by the desorption curves (Figure 5b), almost all adsorbed CO_2 could be wiped out quickly at 3.33 min g^{-1}, followed by the C_2H_2 stream with purity above 99.5%. When the desorption rate decreased at 11.95 min g^{-1}, the heating at 343 K rapidly facilitated the desorption rate of C_2H_2, while no additional CO_2 was released. Benefiting from this strategy, the purity of recovered C_2H_2 raised to above 99.99% after 14.24 min g^{-1}. Noticeably, the collected amounts of C_2H_2 reached 60.1 cm^3 g^{-1} with purity > 99.5% and 33.2 cm^3 g^{-1} with purity > 99.99%. Moreover, the cycling and reusability of adsorbents are critical parameters for practical applications. Successive cycling breakthrough cycles at three flow rates were conducted, and no noticeable deterioration in breakthrough times was observed (Figures S51–S53, Supporting Information). Besides, about 84.5 cm^3 g^{-1} of CO_2 with a purity of 99.99% could be stably obtained in each breakthrough cycle while maintaining high C_2H_2 dynamic uptakes (Figure 5c).

The simulations of PSA processes were further conducted to compare separation performances of SOFOUR-TEPE-Zn,

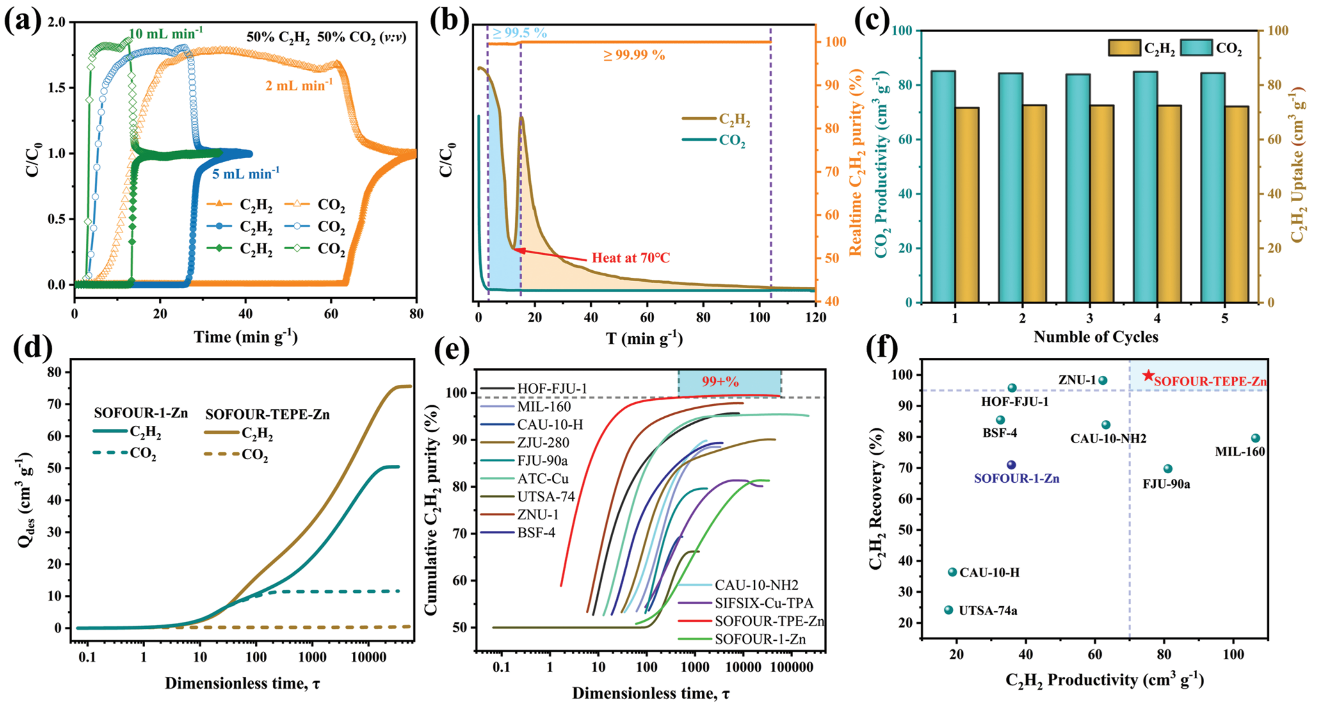

Figure 5. a) The breakthrough curves of SOFOUR-TEPE-Zn for C_2H_2/CO_2 (50/50, v/v) at different flow rates at 298 K. b) The signals of desorbed gases from the breakthrough column. c) The CO_2 productivity and C_2H_2 uptake during cycle breakthrough tests at 2.0 mL min^{-1}. d) Cumulative moles of C_2H_2 and CO_2 recovered, and e) Cumulative C_2H_2 purity recovered from SOFOUR-TEPE-Zn and benchmark adsorbents during simulated counter-current blowdown operations. f) Comparison plot of recovered C_2H_2 productivity and recovery for obtaining 99.5+% C_2H_2.

SOFOUR-1-Zn, and other benchmark MOFs (Figure 5d-e and Figures S21–S31, Supporting Information). The counter-current vacuum blowdown operations were applied to collect C_2H_2 products in a simplified two-bed PSA scheme (Figure S1, Supporting Information).[37,38] In practice, the counter-current blowdown operation will be initiated just before C_2H_2 breaks through in the adsorption column, as indicated by the arrows in Figure S47, Supporting Information. The cumulative moles of recovered C_2H_2 and CO_2 as a function of dimensionless time were plotted in Figure 5d. The recovered amount of C_2H_2 reached 75.7 cm^3 g^{-1} on SOFOUR-TEPE-Zn during the counter-current blowdown process with 100% C_2H_2 recovery, higher than that of SOFOUR-1-Zn (50.4 cm^3 g^{-1}), ZNU-1 (63.4 cm^3 g^{-1}), CAU-10-NH_2 (75.3 cm^3 g^{-1}), UTSA-74 (73.5 cm^3 g^{-1}), and HOF-FJU-1 (37.6 cm^3 g^{-1}, Figure S54 and Table S7, Supporting Information). Noticeably, the amount of recovered CO_2 constantly remained at 0.5 cm^3 g^{-1} on SOFOUR-TEPE-Zn, significantly lower than 11.6 cm^3 g^{-1} on SOFOUR-1-Zn, indicating a much higher C_2H_2 purity during counter-current blowdown process.[38,44]

As shown in Figure 5e, a record-high C_2H_2 purity of 99+% could be achieved at $\tau = 412.1$ on SOFOUR-TEPE-Zn, and the final C_2H_2 purity could reach 99.34% with 100% C_2H_2 recovery, outperforming that of SOFOUR-1-Zn (81.31%), MIL-160 (88.47%), CAU-10-NH_2 (89.82%), ZJU-280 (90.06%), FJU-90a (79.62%), UTSA-74 (66.19%), and ZNU-1 (97.80%, Figure S54 and Table S7, Supporting Information). To produce polymer-degree C_2H_2 (purity > 99.5%), certain amounts of gas products will be released before collection in the counter-current blowdown process, which will inevitably lead to the reduction of gas recovery. Therefore, we further compared the gas recovery on the basis of obtaining 99.5+% purity C_2H_2 (Table S8, Supporting Information). As shown in Figure 5f, SOFOUR-TEPE-Zn still maintained a high gas recovery of 99.82% with a C_2H_2 productivity of 75.5 cm^3 g^{-1}, outperforming SOFOUR-1-Zn (70.97% and 35.8 cm^3 g^{-1}), HOF-FJU-1 (95.81% and 36.1 cm^3 g^{-1}), ZNU-1 (98.22% and 62.3 cm^3 g^{-1}), BSF-4 (85.45% and 32.7 cm^3 g^{-1}), UTSA-74 (24.18% and 17.7 cm^3 g^{-1}), FJU-90a (69.73% and 81.1 cm^3 g^{-1}), and MIL-160 (79.61% and 106.4 cm^3 g^{-1}).

3. Conclusion

In summary, a dense electronegative pore environment was constructed in SOFOUR-TEPE-Zn, achieving highly selective recognition for C_2H_2 and benchmark C_2H_2/CO_2 separation performances. Noticeably, SOFOUR-TEPE-Zn exhibited a record-high C_2H_2/CO_2 selectivity (16 833) with leading C_2H_2 adsorption capacity (89.1 cm^3 g^{-1}) at 298 K and 1.0 bar. Dynamic breakthrough experiments confirmed clean separations of equimolar C_2H_2/CO_2 gas-mixtures. Meanwhile, 60.1 cm^3 g^{-1} C_2H_2 of 99.5% purity or 33.2 cm^3 g^{-1} C_2H_2 of 99.99% purity can be recovered during desorption using stepped purging and mild heating. The simulated PSA processes demonstrated high C_2H_2 productivity of 75.5 cm^3 g^{-1} C_2H_2 of 99.5% purity could be produced with 99.82% C_2H_2 recovery. DFT-D and GCMC simulations identified the favorable C_2H_2 adsorption sites in the electronegative pore environments created by SO_4^{2-} anions and TEPE ligands.

Supporting Information

Supporting Information is available from the Wiley Online Library or from the author.

Acknowledgements

This study was supported by the National Natural Science Foundation of China (No. 22008099, 22008101, 22108243, and 22168023) and Natural Science Foundation of Jiangxi Province (No. 20224ACB204003). The CCDC No. 2240118 contains the supplementary crystallographic data for this paper. These data can be obtained free of charge from the Cambridge Crystallographic Data Centre via www.ccdc.cam.ac.uk/data_request/cif.

Conflict of Interest

The authors declare no conflict of interest.

Data Availability Statement

The data that support the findings of this study are available in the supplementary material of this article.

Keywords

adsorptive separation, electrostatic separation, metal-organic frameworks, pore environment modification

Received: November 9, 2022
Revised: February 14, 2023
Published online: March 29, 2023

---

[1] K. Weissermel, H.-J. Arpe, in *Industrial Organic Chemistry*, Wiley-VCH, Weinheim **2003**, p. 91.
[2] J. Li, M. F. Stephanopoulos, Y. Xia, *Chem. Rev.* **2020**, *120*, 11699.
[3] D. S. Sholl, R. P. Lively, *Nature* **2016**, *532*, 435.
[4] S. Sircar, *Ind. Eng. Chem. Res.* **2002**, *41*, 1389.
[5] J. R. Li, R. J. Kuppler, H. C. Zhou, *Chem. Soc. Rev.* **2009**, *38*, 1477.
[6] R. Matsuda, R. Kitaura, S. Kitagawa, Y. Kubota, R. V. Belosludov, T. C. Kobayashi, H. Sakamoto, T. Chiba, M. Takata, Y. Kawazoe, Y. Mita, *Nature* **2005**, *436*, 238.
[7] X. Zhao, Y. Wang, D.-S. Li, X. Bu, P. Feng, *Adv. Mater.* **2018**, *30*, 1705189.
[8] W. J. F. Trenholme, D. I. Kolokolov, M. Bound, S. P. Argent, J. A. Gould, J. Li, S. A. Barnett, A. J. Blake, A. G. Stepanov, E. Besley, T. L. Easun, S. Yang, M. Schroder, *J. Am. Chem. Soc.* **2021**, *143*, 3348.
[9] Z. Chen, K. O. Kirlikovali, P. Li, O. K. Farha, *Acc. Chem. Res.* **2022**, *55*, 579.
[10] J. Jiao, W. Gong, X. Wu, S. Yang, Y. Cui, *Coord. Chem. Rev.* **2019**, *385*, 174.
[11] J. Pei, K. Shao, J. X. Wang, H. M. Wen, Y. Yang, Y. Cui, R. Krishna, B. Li, G. Qian, *Adv. Mater.* **2020**, *32*, 1908275.
[12] F. Luo, C. Yan, L. Dang, R. Krishna, W. Zhou, H. Wu, X. Dong, Y. Han, T. L. Hu, M. O'Keeffe, L. Wang, M. Luo, R. B. Lin, B. Chen, *J. Am. Chem. Soc.* **2016**, *138*, 5678.
[13] Z. Niu, X. Cui, T. Pham, G. Verma, P. C. Lan, C. Shan, H. Xing, K. A. Forrest, S. Suepaul, B. Space, A. Nafady, A. M. Al-Enizi, S. Ma, *Angew. Chem., Int. Ed. Engl.* **2021**, *60*, 5283.
[14] Y. L. Peng, T. Pham, P. Li, T. Wang, Y. Chen, K. J. Chen, K. A. Forrest, B. Space, P. Cheng, M. J. Zaworotko, Z. Zhang, *Angew. Chem., Int. Ed. Engl.* **2018**, *57*, 10971.
[15] U. Kokcam-Demir, A. Goldman, L. Esrafili, M. Gharib, A. Morsali, O. Weingart, C. Janiak, *Chem. Soc. Rev.* **2020**, *49*, 2751.
[16] L. Zhang, K. Jiang, L. Yang, L. Li, E. Hu, L. Yang, K. Shao, H. Xing, Y. Cui, Y. Yang, B. Li, B. Chen, G. Qian, *Angew. Chem., Int. Ed. Engl.* **2021**, *60*, 15995.
[17] R. B. Lin, L. Li, H. Wu, H. Arman, B. Li, R. G. Lin, W. Zhou, B. Chen, *J. Am. Chem. Soc.* **2017**, *139*, 8022.
[18] M. Shivanna, K. I. Otake, B. Q. Song, L. M. van Wyk, Q. Y. Yang, N. Kumar, W. K. Feldmann, T. Pham, S. Suepaul, B. Space, L. J. Barbour, S. Kitagawa, M. J. Zaworotko, *Angew. Chem., Int. Ed. Engl.* **2021**, *60*, 20383.
[19] L. Wang, N. Xu, Y. Hu, W. Sun, R. Krishna, J. Li, Y. Jiang, S. Duttwyler, Y. Zhang, *Nano Res.* **2023**, *16*, 3536.
[20] D. D. Zhou, J. P. Zhang, *Acc. Chem. Res.* **2022**, *55*, 2966.
[21] Y. Yang, H. Zhang, Z. Yuan, J. Q. Wang, F. Xiang, L. Chen, F. Wei, S. Xiang, B. Chen, Z. Zhang, *Angew. Chem., Int. Ed. Engl.* **2022**, *61*, 202207579.
[22] Y. Liu, J. Liu, H. Xiong, J. Chen, S. Chen, Z. Zeng, S. Deng, J. Wang, *Nat. Commun.* **2022**, *13*, 5515.
[23] Y. Xie, H. Cui, H. Wu, R. B. Lin, W. Zhou, B. Chen, *Angew. Chem., Int. Ed. Engl.* **2021**, *60*, 9604.
[24] L. Wang, W. Sun, Y. Zhang, N. Xu, R. Krishna, J. Hu, Y. Jiang, Y. He, H. Xing, *Angew. Chem., Int. Ed. Engl.* **2021**, *60*, 22865.
[25] S. Mukherjee, Y. He, D. Franz, S. Q. Wang, W. R. Xian, A. A. Bezrukov, B. Space, Z. Xu, J. He, M. J. Zaworotko, *Chemistry* **2020**, *26*, 4923.
[26] O. T. Qazvini, R. Babarao, S. G. Telfer, *Nat. Commun.* **2021**, *12*, 197.
[27] Y. Shi, Y. Xie, H. Cui, Y. Ye, H. Wu, W. Zhou, H. Arman, R. B. Lin, B. Chen, *Adv. Mater.* **2021**, *33*, 2105880.
[28] Z. Zhang, S. B. Peh, R. Krishna, C. Kang, K. Chai, Y. Wang, D. Shi, D. Zhao, *Angew. Chem., Int. Ed. Engl.* **2021**, *60*, 17198.
[29] Y. Y. Xue, X. Y. Bai, J. Zhang, Y. Wang, S. N. Li, Y. C. Jiang, M. C. Hu, Q. G. Zhai, *Angew. Chem., Int. Ed. Engl.* **2021**, *60*, 10122.
[30] Y. Feng, Z. Wang, W. Fan, Z. Kang, S. Feng, L. Fan, S. Hu, D. Sun, *J. Mater. Chem. A* **2020**, *8*, 13132.
[31] D. Sensharma, D. J. O'Hearn, A. Koochaki, A. A. Bezrukov, N. Kumar, B. H. Wilson, M. Vandichel, M. J. Zaworotko, *Angew. Chem., Int. Ed. Engl.* **2022**, *61*, 202116145.
[32] G. D. Wang, R. Krishna, Y. Z. Li, W. J. Shi, L. Hou, Y. Y. Wang, Z. Zhu, *Angew. Chem., Int. Ed. Engl.* **2022**, *61*, 202213015.
[33] X. Zhang, R.-B. Lin, H. Wu, Y. Huang, Y. Ye, J. Duan, W. Zhou, J.-R. Li, B. Chen, *Chem. Eng. J.* **2022**, *431*, 134184.
[34] L. Liu, Z. Yao, Y. Ye, Y. Yang, Q. Lin, Z. Zhang, M. O'Keeffe, S. Xiang, *J. Am. Chem. Soc.* **2020**, *142*, 9258.
[35] L. Yang, L. Yan, Y. Wang, Z. Liu, J. He, Q. Fu, D. Liu, X. Gu, P. Dai, L. Li, X. Zhao, *Angew. Chem., Int. Ed. Engl.* **2021**, *60*, 4570.
[36] J. Wang, Y. Zhang, Y. Su, X. Liu, P. Zhang, R. B. Lin, S. Chen, Q. Deng, Z. Zeng, S. Deng, B. Chen, *Nat. Commun.* **2022**, *13*, 200.
[37] R. Krishna, *RSC Adv.* **2017**, *7*, 35724.
[38] R. Krishna, *ACS Omega* **2020**, *5*, 16987.
[39] P. Nugent, Y. Belmabkhout, S. D. Burd, A. J. Cairns, R. Luebke, K. Forrest, T. Pham, S. Ma, B. Space, L. Wojtas, M. Eddaoudi, M. J. Zaworotko, *Nature* **2013**, *495*, 80.
[40] H. Schobert, *Chem. Rev.* **2014**, *114*, 1743.
[41] Q. Zhang, J. Wang, T. Wang, *Ind. Eng. Chem. Res.* **2016**, *55*, 8383.
[42] Y. Ye, Z. Ma, R. B. Lin, R. Krishna, W. Zhou, Q. Lin, Z. Zhang, S. Xiang, B. Chen, *J. Am. Chem. Soc.* **2019**, *141*, 4130.
[43] Y. P. Li, Y. Wang, Y. Y. Xue, H. P. Li, Q. G. Zhai, S. N. Li, Y. C. Jiang, M. C. Hu, X. Bu, *Angew. Chem., Int. Ed. Engl.* **2019**, *58*, 13590.
[44] R. Krishna, *RSC Adv.* **2015**, *5*, 52269.

ADVANCED MATERIALS

Supporting Information

for *Adv. Mater.,* DOI: 10.1002/adma.202210415

Engineering Pore Environments of Sulfate-Pillared Metal-Organic Framework for Efficient C_2H_2/CO_2 Separation with Record Selectivity

*Xing Liu, Peixin Zhang, Hanting Xiong, Yan Zhang, Ke Wu, Junhui Liu, Rajamani Krishna, Jingwen Chen, Shixia Chen, Zheling Zeng, Shuguang Deng, and Jun Wang**

Supplementary Information

Engineering Pore Environments of Sulfate-pillared Metal-Organic Framework for Efficient C_2H_2/CO_2 Separation with Record Selectivity

Xing Liu[a], Peixin Zhang[a], Hanting Xiong[a], Yan Zhang[a], Ke Wu[a], Junhui Liu[a], Rajamani Krishna[b], Jingwen Chen[a], Shixia Chen[a], Zheling Zeng[a], Shuguang Deng[c], Jun Wang[a*]

a. Chemistry and Chemical Engineering School, Nanchang University, Nanchang, Jiangxi 330031, China.
b. Van't Hoff Institute for Molecular Sciences, University of Amsterdam, Science Park 904, 1098 XH Amsterdam, Netherlands.
c. School for Engineering of Matter, Transport and Energy, Arizona State University, Tempe, Arizona 85287, USA.

*Corresponding authors:

Dr. Jun Wang, E-mail: jwang7@ncu.edu.cn

Materials

All reagents were purchased from commercial companies and used without further purification. ZnSO4·7H2O (99.98%, Aladdin), 1,1,2,2-tetra(pyridin-4-yl) ethene ($C_{22}H_{16}N_4$, 99+%, Extension), and methanol (CH_4O, anhydrous, 99.9%, Aladdin). N_2 (99.999%), acetylene (C_2H_2, 99.99%), carbon dioxide (CO_2, 99.99%), He (99.999%), and mixed gas-mixtures of C_2H_2/CO_2 (50/50, *v/v*), were purchased from Shanghai Wei Chuang Gas Co., Ltd (China).

Synthesis of SOFOUR-TEPE-Zn

Typically, $ZnSO_4·7H_2O$ (0.3 mmol) was added to a solution of TEPE (0.3 mmol) in 20 mL MeOH and stirred at room temperature overnight. SOFOUR-TEPE-Zn·xMeOH was obtained as a white microcrystalline powder, which was isolated by filtration, washed with MeOH three times, and dried 6 h in a vacuum oven at 333 K. (yield: 1527 mg as synthesized, 1245 mg as activated).

Details for Rietveld refinement

The initial structure for SOFOUR-TEPE-Zn was referred to the reported work (CCDC identifier: 2105435). We applied the EXPO2014 software to conduct the Rietveld refinement, the 2θ range of 5~60° was used for the refinement. Chebyshev (Background Function) and Pseudo-Voigt (Peak Shape Functions) were applied to refine the structure until the R_{wp} value converged and the overlay of the observed with refined profiles showed good agreement. Unit cell parameters and fitting reliability are listed in Table S2, and we have deposited the CIF in the CCDC database with an identifier number of 2240118.

^{1}H NMR and ^{13}C NMR spectroscopy analysis of digested MOF samples NMR measurement:

For ^{1}H NMR and ^{13}C NMR spectroscopy, the activated SOFOUR-TEPE-Zn was digested using the following protocol: 500 μL of 20% DCl in D_2O mixed with 1000 μL of DMSO-d_6 to give a DCl/DMSO-d_6 stock solution. About 5 mg of SOFOUR-TEPE-Zn or TEPE ligands was digested in 450 μL of this stock solution. Spectra were acquired immediately on a Bruker Spectrometer following dissolution.

Ultimate element analysis

The contents of C, H, N, S, and O elements were determined by an Elementar Vario MICRO elemental analyzer with an O measurement mode. In detail, about 2 mg samples were weighed and wrapped in a tin foil ark, then placed in the sample tray. Using high-purity helium as the carrier gas, the content of each element was detected by a TCD detector in CHNS and O mode, respectively.

Scanning electron microscope (SEM)

The sample was directly glued to the conductive adhesive, and the gold spraying for 45s (10mA) was conducted on Oxford Quorum SC7620 sputtering coater. The SEM images were recorded on a ZEISS Sigma 300 scanning electron microscope with an accelerated voltage of 3kV.

Transmission electron microscope (TEM) and energy dispersive X-ray spectroscopy (EDX) elemental mapping

Transmission electron microscope images were obtained by a Thermo Fisher Talos F200S G2 microscope with selected area electron diffraction (SAED) patterns. EDX analyses were performed with a Ge detector and careful calibration using standards permitted quantitative analyses of major elements.

X-ray Photoelectron Spectroscopy (XPS)

The XPS spectra of SOFOUR-TEPE-Zn were collected by Thermo Scientific K-Alpha XPS instrument. The sample chamber was vacuumed less than 2.0×10^{-7} mbar before each test. The spot size was 400 μm, the working voltage was 12 kV, and the filament current was 6 mA. The full spectrum scanning energy was 150 eV with a step size of 1 eV. The narrow-spectrum scanning energy was 50 eV with a step size of 0.1 eV.

Fourier transform infrared spectroscopy (FT-IR)

In a dry environment, an appropriate amount of SOFOUR-TEPE-Zn and dried potassium bromide (KBr) powder were added into a mortar, thoroughly ground and transferred to a tablet press. The background was first collected during the test, and then the infrared spectrum of the sample was collected. The resolution was 4 cm^{-1}, the number of scans was 32, and the test wave number was 400-4000 cm^{-1}.

Gas adsorption measurements

Equilibrium and kinetic adsorptions of C_2H_2, and CO_2 at 273, 298 K, and 323 K were measured on Micromeritics 3 Flex adsorption apparatus (Micromeritics Instruments, USA). To remove all the guest solvents in the framework, the fresh powder samples were evacuated under a high vacuum at 333 K for 6 h. The Brunauer-Emmett-Teller (BET) surface area was calculated using the adsorption branch with the relative pressure P/P_0 in the range of 0.05 to 0.3. The total pore volume (V_{tot}) was calculated based on the adsorbed amount of CO_2 at the P/P_0 of 0.99. The helium gas was used to determine the free space of the system. The sample was degassed for 6 h between each measurement.

Fitting of unary isotherm data

The unary isotherms for C_2H_2 measured at three different temperatures 273 K, 298 K, and 323 K in SOFOUR-TEPE-Zn were fitted with excellent accuracy using either the dual-site Langmuir model, where we distinguish two distinct adsorption sites A and B:

$$q = \frac{q_{sat,A} b_A p}{1 + b_A p} + \frac{q_{sat,B} b_B p}{1 + b_B p} \tag{S1}$$

In eq (S1), the Langmuir parameters b_A, b_B are both temperature dependent

$$b_A = b_{A0}\, exp\left(\frac{E_A}{RT}\right); \quad b_B = b_{B0}\, exp\left(\frac{E_B}{RT}\right) \tag{S2}$$

In eq (S2), E_A, E_B are the energy parameters associated with sites A, and B, respectively.

The unary isotherms for CO_2 measured at three different temperatures 273 K, 298 K, and 323 K in SOFOUR-TEPE-Zn were fitted with excellent accuracy using the single-site Langmuir model.

$$q = \frac{q_{sat,A} b_A p}{1 + b_A p} \tag{S3}$$

The unary isotherm fit parameters for C_2H_2 and CO_2 in SOFOUR-TEPE-Zn are provided in Table S1.

Isosteric heat of adsorption

The isosteric heat of adsorption, Q_{st}, is defined as

$$Q_{st} = -RT^2 \left(\frac{\partial \ln p}{\partial T}\right)_q \tag{S4}$$

where the derivative in the right member of eq (S4) is determined at constant adsorbate loading, *q*.

IAST calculations

For screening MOFs for separation of binary mixtures of components 1 and 2, the adsorption selectivity, S_{ads}, is defined by

$$S_{ads} = \frac{q_1/q_2}{y_{10}/y_{20}} \tag{S5}$$

In eq (S5), y_{10}, y_{20} are the mole fractions of the bulk gas phase mixture.

The C_2H_2 (1)/CO_2 (2) mixture separations are envisaged to be carried out in fixed bed adsorbers. In such devices, the separations are dictated by adsorption selectivity and uptake capacity. Using the shock wave model for fixed-bed adsorbers, Krishna[1, 2] has suggested that the appropriate metric is the separation potential, Δq_1. The appropriate expression describing the productivity of pure C_2H_2 in the desorption phase of fixed-bed operations is

$$\Delta q_1 = q_1 - q_2 \frac{y_{10}}{y_{20}} \tag{S6}$$

In eq (S6) y_{10}, y_{20} are the mole fractions of the feed mixture during the adsorption cycle. In the derivation of eq (S6), it is assumed that the concentration "fronts" traversed the column in the form of shock waves during the desorption cycle. The molar loadings q_1, q_2 of the two components are determined using the Ideal Adsorbed Solution Theory (IAST) of Myers and Prausnitz using the unary isotherm fits as data inputs.[3] The physical significance of Δq_1 is the maximum productivity of pure C_2H_2(1) that is achievable in PSA operations.

Calculation of kinetic adsorption

The kinetic adsorption curves of C_2H_2 and CO_2 for SOFOUR-TEPE-Zn were measured on Intelligent Gravimetric Analyzer (IGA-100, HIDEN).

The diffusional time constants (D', D/r2) were calculated by the short-time solution of the diffusion equation assuming a step change in the gas-phase concentration[4], clean beds initially, and micropore diffusion control:

$$\frac{M_t}{M_e} = \frac{6}{\sqrt{\pi}} \cdot \sqrt{\frac{D}{r^2} \cdot t} \tag{S7}$$

Where M_t is the gas uptake at time t(s), M_e is the gas uptake at equilibrium ($cm^3\ g^{-1}$), D ($m^2\ s^{-1}$) is the diffusivity and r (m) is the radius of the equivalent spherical particle. The slopes of M_t/M_e versus $t^{1/2}$ are derived from the fitting of the plots at 500 mbar and 298 K.

Transient breakthrough experiments and simulations

The breakthrough experiments were performed on a self-assembly device. Typically, the activated SOFOUR-TEPE-Zn (0.5145 g) was packed into a stainless-steel column (4 mm inner diameter × 30mm). The column was first purged with a He flow (10 mL min^{-1}) at room temperature for 6 h before breakthrough measurements. The binary C_2H_2/CO_2 (50/50, *v/v*) gas-mixture was introduced at fixed flow rates of 2 mL min^{-1}, 5 mL min^{-1}, and 10 mL min^{-1}, respectively. The outlet gas from the column was monitored using mass s1pectrometry (Hidden, UK), and an attached mass flow controller (Seven Star, MC-2SCCM-D) was used to control the gas flow. After each breakthrough measurement, the columns packed with samples were regenerated by purging dry He gas (10 mL min^{-1}) at room temperature.

Transient breakthrough simulations were carried out for the same operating conditions as in the three experimental data sets, using the methodology described in earlier publications.[1, 2, 5-7] In these simulations, intra-crystalline diffusion influences are ignored.

Adsorption/desorption cycles

The desired ethyne product is available in the blowdown phase of the simplified scheme shown in Figure S1. To compare the separation performance of SOFOUR-TEPE-Zn with other materials with excellent properties, we conducted simulations of both adsorption and counter-current vacuum blow-down operations. For these simulations we choose: length of packed bed, L = 0.3 m; cross-sectional area, A = 1 m^2; superficial gas velocity at the entrance to the bed, $u_0 = 0.04$ m s^{-1}; voidage of the packed bed, ε = 0.4. The interstitial gas velocity $v = \frac{u}{\varepsilon}$. The total volume of the bed is $V_{bed} = LA$. The volume of zeolite or MOF used in the simulations is $V_{ads} = LA(1-\varepsilon)$.

It is important to note that the volume of adsorbent, V_{ads}, includes the pore volume of the adsorbent material. If ρ is the framework density, the mass of the adsorbent in the bed is:

$$m_{ads} = (1-\varepsilon)\times(L\ \mathrm{m})\times(A\ \mathrm{m}^2)\times(\rho\ \mathrm{kg\ m^{-3}})\ \mathrm{kg}. \tag{S8}$$

The dimensionless concentrations in the exit, c_i/c_{i0} are plotted as a function of the parameter:

$$\frac{(Q_0 = \text{flow rate mL min}^{-1})\times(\text{time in min})}{(\text{g MOF packed in tube})} = \frac{Q_0 t}{m_{ads}} = \mathrm{mL\ g^{-1}}. \tag{S9}$$

In our simulations, a deep vacuum (= 2 Pa) was applied. Since the vacuum pump characteristics are unknown, it is arbitrarily assumed that the interstitial velocity in the fixed bed is maintained at $v = \frac{u}{\varepsilon} = 0.1 \quad \mathrm{m\ s^{-1}}$. Desorption is a much slower process, and the time required for the total recovery of adsorbed components is significant.

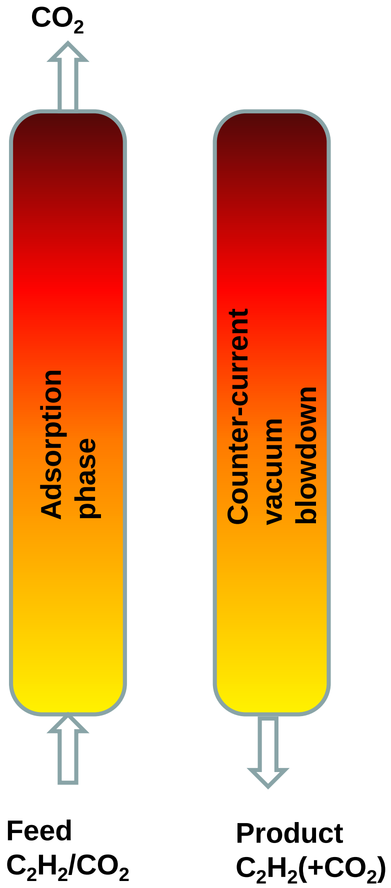

Figure S1. Sequential steps in the operation of a fixed-bed adsorber in a simplified two-bed scheme for C_2H_2(1)/CO_2(2) separation.[8]

Density functional theory calculations

First-principles density functional theory (DFT) calculations were performed using Materials Studio’s CASTEP code. All calculations were conducted under the generalized gradient approximation (GGA) with Perdew-Burke-Ernzerhof (PBE). The optimized structures are in great consistency with the experimentally determined crystal structures. The energy, force, and displacement convergence criteria were set as 1×10^{-5} eV, 3×10^{-2} eV, and 1×10^{-3} Å, respectively. Single point energy calculations with the same parameters using Dmol^3 were performed on optimized SOFOUR-TEPE-Zn. The electron density data obtained from these calculations were used to construct the 0.015 e^{-} $Å^{-3}$ electron density isosurfaces of the C_2H_2 and CO_2 molecules, while the electron density data of both frameworks were used to construct the 0.15 e^{-} $Å^{-3}$ electron density isosurfaces, with a grid interval of 0.1 Å. The calculated electrostatic potential for SOFOUR-TEPE-Zn and C_2H_2 and CO_2 molecules were then mapped onto their electron density isosurfaces. A semiempirical addition of dispersive forces to conventional DFT was included in the calculation to account for van der Waals interactions. Cutoff energy of 600 eV and a 2 × 2 × 3 k-point mesh were enough for the total energy coverage within 0.01 meV $atom^{-1}$. The structures of the synthesized materials were first optimized from the reported crystal structures. To obtain the binding energy, the pristine structure and an isolated gas molecule placed in a supercell (with the same cell dimensions as the pristine crystal structure) were optimized and relaxed as references. C_2H_2 and CO_2 gas molecules were then introduced to different locations of the channel pore, followed by a full structural relaxation. The static binding energy was calculated by the equation $E_B = E\ (gas) + E\ (adsorbent) - E\ (adsorbent + gas)$.

Grand Canonical Monte Carlo (GCMC) calculations

All the GCMC simulations were performed in MS 2020 package. The crystal structure of the SOFOUR-TEPE-Zn was chosen after the DFT geometry optimization. The framework and the individual C_2H_2 and CO_2 were considered rigid during the simulation. The charges for atoms of the SOFOUR-TEPE-Zn and gas components were derived from the Muliken method. The simulations adopted the fixed pressure task, Metropolis method in the sorption module, the force field parameters of metal atoms are from the UFF force field, while those of non-metallic atoms are from Dreiding force field. The interaction energy between the adsorbed molecules and the framework was computed through the Coulomb and Lennard-Jones 6-12 (LJ) potentials. The cutoff radius was chosen 15.5 Å for LJ potential, and the electrostatic interactions were handled using the Ewald summation method. The loading steps and the equilibration steps were 5×10^{7}, the production steps were 5×10^{7}.

Structural stability tests

Powder X-ray diffraction (PXRD) was collected on a PANalytical Empyrean Series 2 diffractometer with Cu Kα radiation ($\lambda = 1.540598$ Å), which operated at 40 kV, 40 mA and a scan speed of 0.0167°, a scan time of 15 s per step, and 2θ ranging from 5 to 60° at room temperature. The thermogravimetric analysis (TGA) data were performed on a NETZSCH Thermogravimetric Analyzer (STA2500) from 25 to 800 °C with a heating rate of 10 °C/min under an N_2 atmosphere. Solvent stability tests were performed by placing 100 mg samples in 20 mL vials containing 15 mL of organic solvent for one week at ambient temperature. Then, the solid was separated by filtration and subsequently activated at 343 K for 6 h, and PXRD tests characterized the structure of materials.

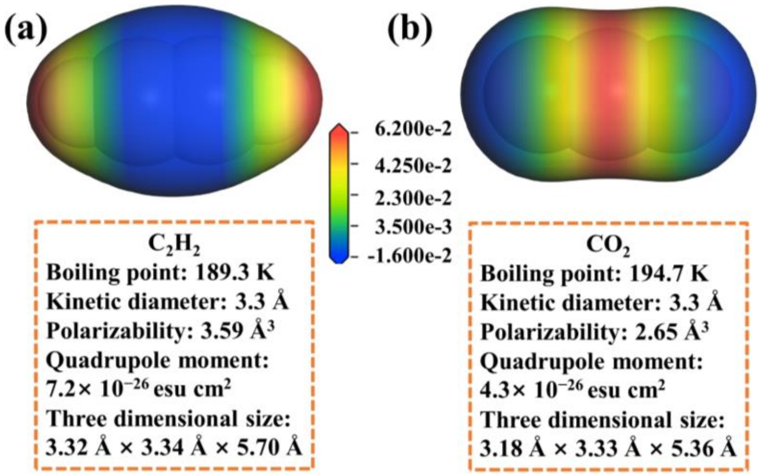

Figure S2. Isosurface maps of the molecular electrostatic potential (MESP), molecular sizes, and physical properties for (a) C_2H_2 and (b) CO_2. Red and blue colors represent the positive and negative part of MESP, respectively.

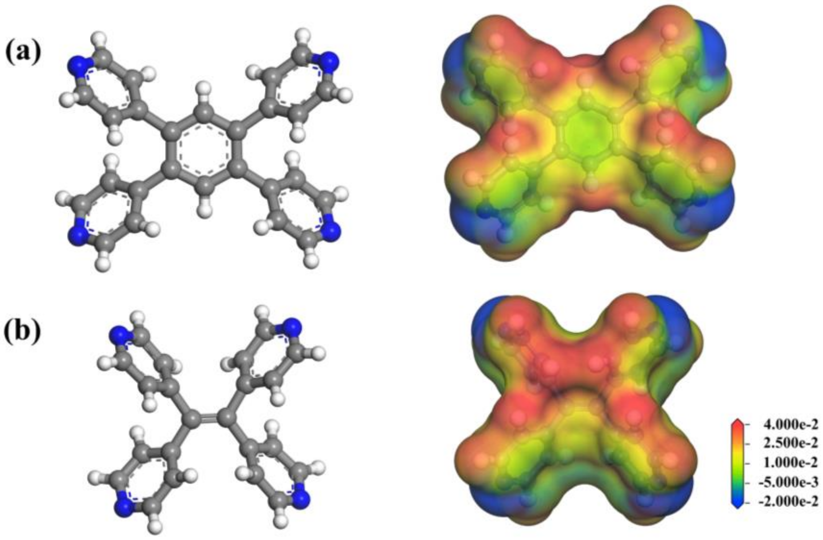

Figure S3. The molecule structure and MESP mapping for (a) TEPB and (b) TEPE organic ligand.

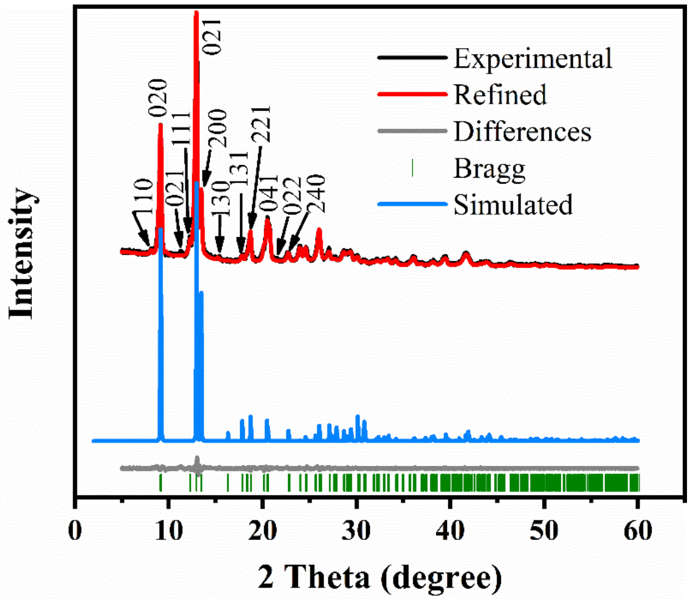

Figure S4. Rietveld refinement plot and PXRD patterns of as-synthesized SOFOUR-TEPE-Zn.

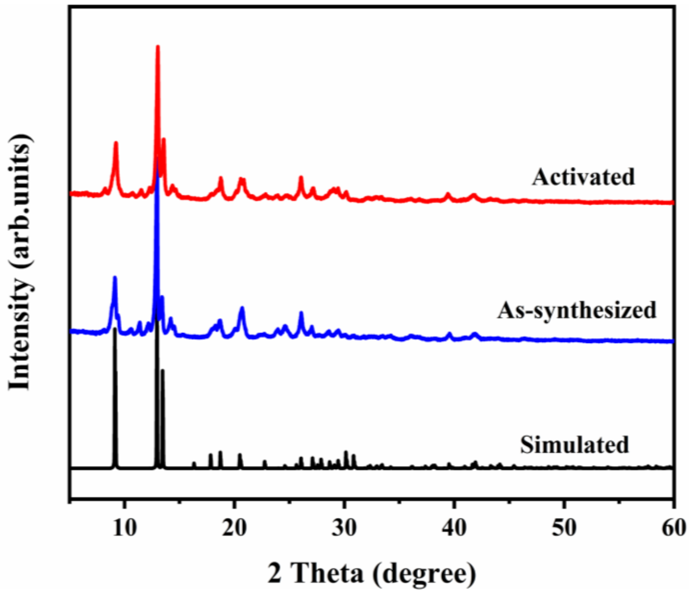

Figure S5. PXRD patterns of SOFOUR-TEPE-Zn under different conditions.

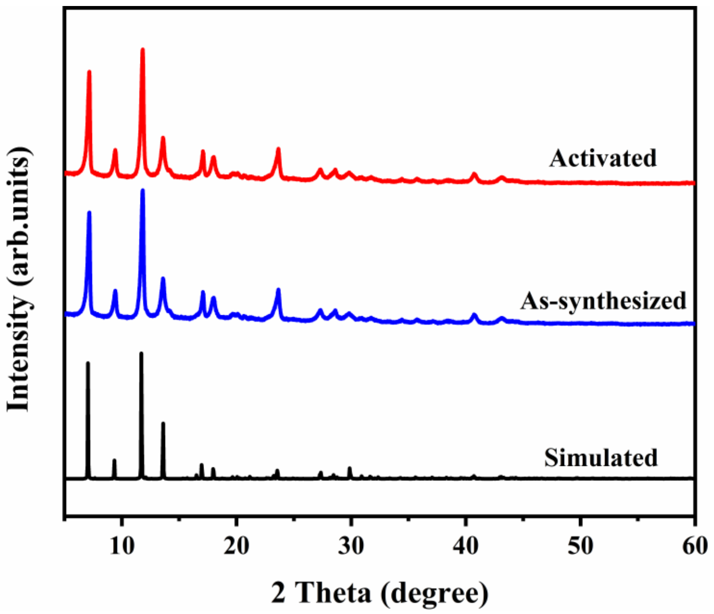

Figure S6. PXRD patterns of SOFOUR-1-Zn under different conditions.

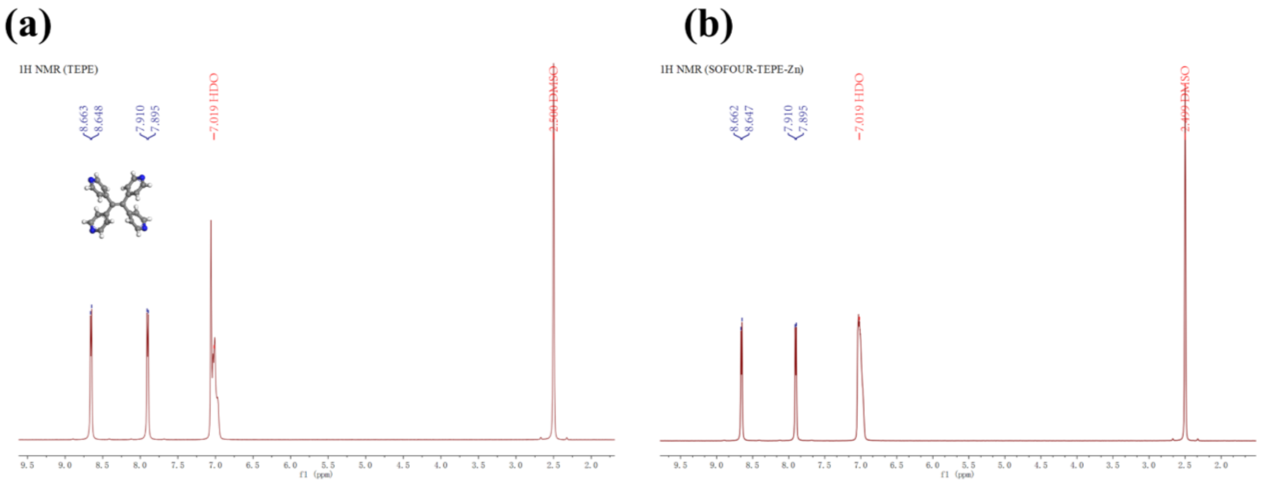

Figure S7. ^{1}H NMR spectrums of digested (a) TEPE ligands and (b) SOFOUR-TEPE-Zn.

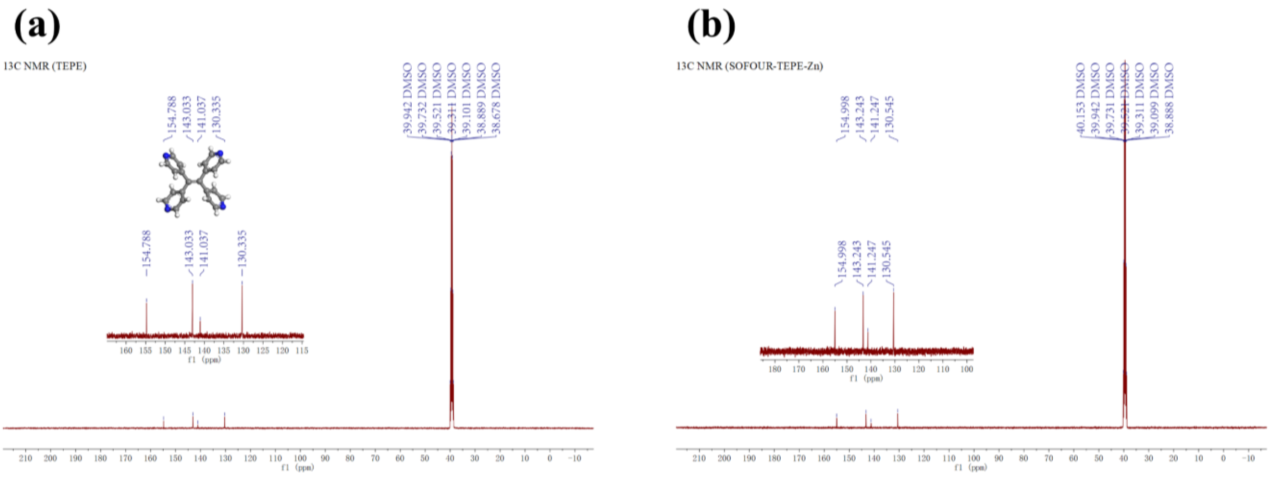

Figure S8. ^{13}C NMR spectrums of digested (a) TEPE ligands and (b) SOFOUR-TEPE-Zn.

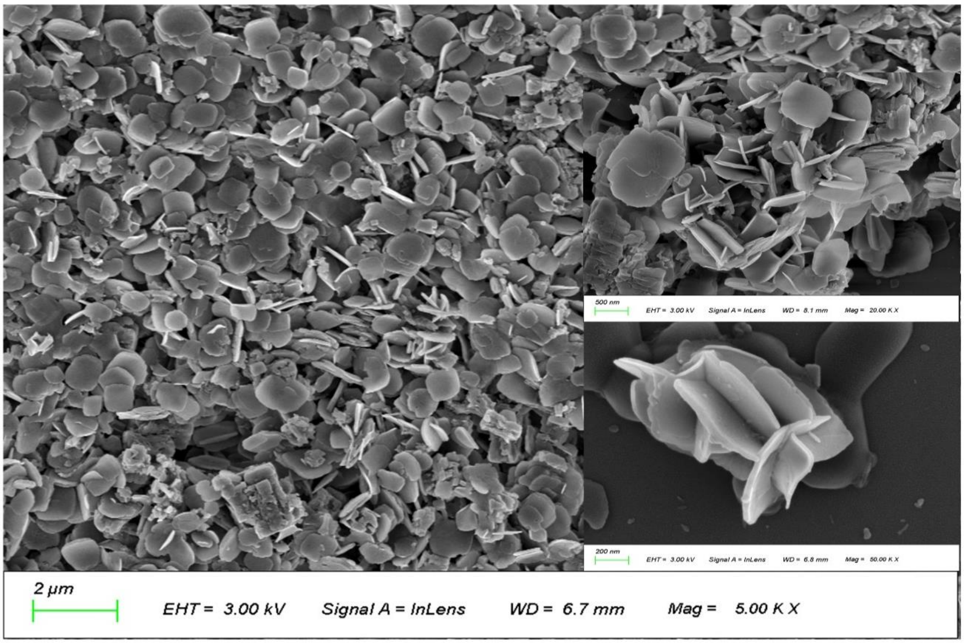

Figure S9. SEM image of SOFOUR-TEPE-Zn with the corresponding enlarged images.

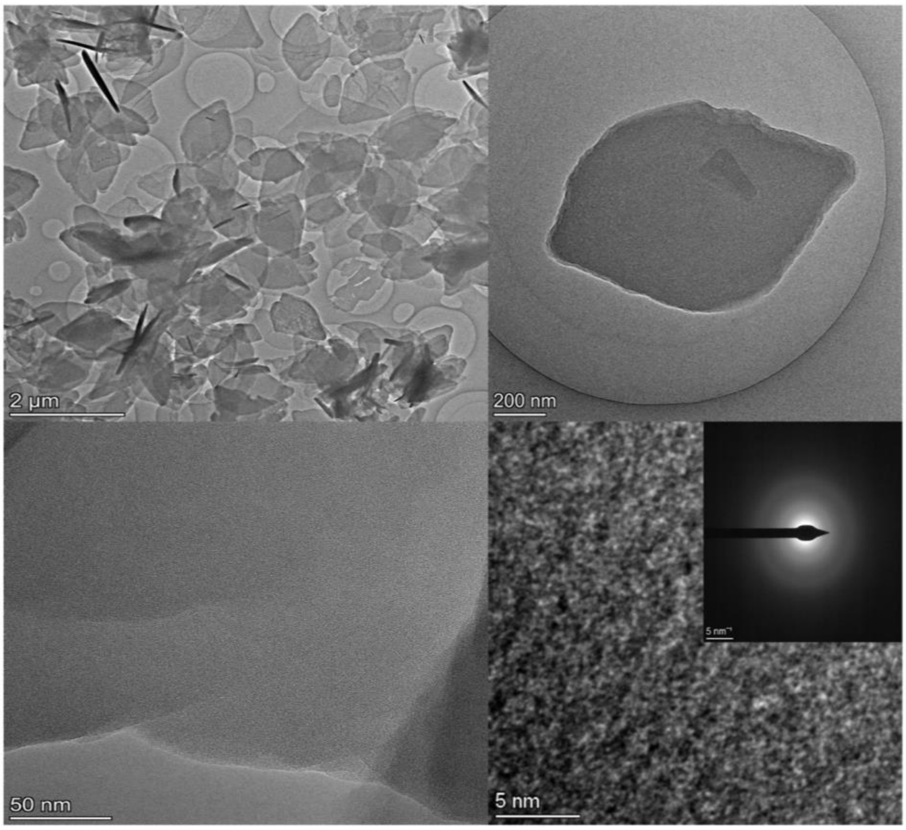

Figure S10. TEM images of SOFOUR-TEPE-Zn with the corresponding enlarged images. Note: No obvious SAED pattern was observed due to the intolerance to the electron bombardment.

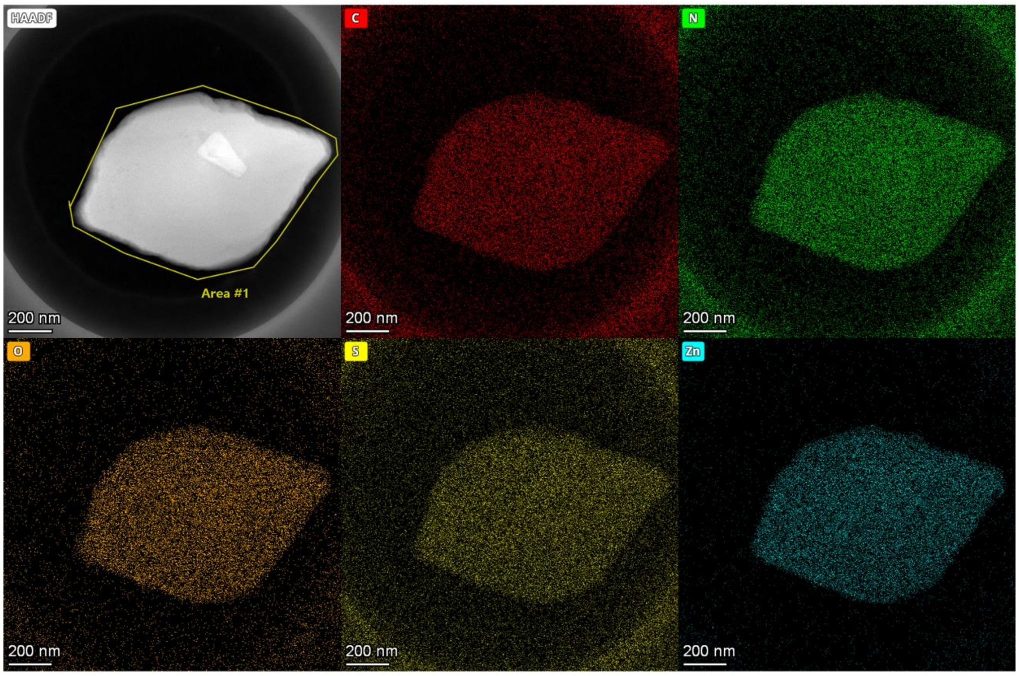

Figure S11. TEM-EDX elemental mapping of SOFOUR-TEPE-Zn.

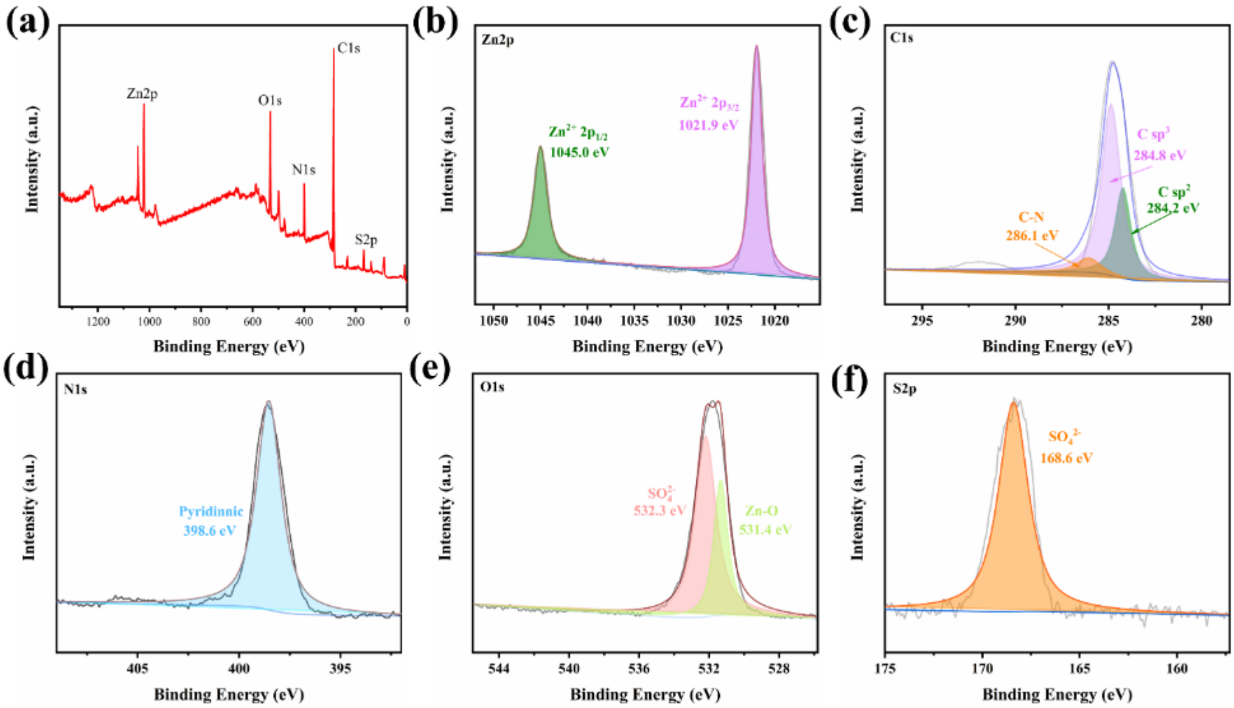

Figure S12. Wide and high-resolution XPS spectra of SOFOUR-TEPE-Zn.

The wide XPS survey illustrated that SOFOUR-TEPE-Zn contained C, N, O, S, and Zn elements (Figure S12a). All the measured spectra are calibrated in energy at the binding energy (BE) of C 1s (284.8 eV) to adjust the surface charging effects. The high-resolution Zn 2p spectra displayed two peaks at around 1045.0 and 1021.9 eV, corresponding to the Zn $2p_{1/2}$ and Zn $2p_{3/2}$ states, respectively (Figure S12b).[9] The high-resolution C 1s spectrum could be divided into three peaks, including the peaks of 284.2 and 286.1 eV for the sp^2 C and sp^3 C, and the peak at 286.1 eV for the C-N bond (Figure S12c).[10] The high-resolution N 1s spectrum displayed the characteristic peak of pyridinic-N at 398.6 eV (Figure S12d).[11] The high-resolution O 1s spectrum could be divided into two peaks at 523.3 and 531.4eV, attributing to the sulfate-O and Zn-O bonds (Figure S12e).[12-14] The peak at 168.6 eV in the high-resolution S 2p spectrum belonged to the sulfate-S (Figure S12f).[15]

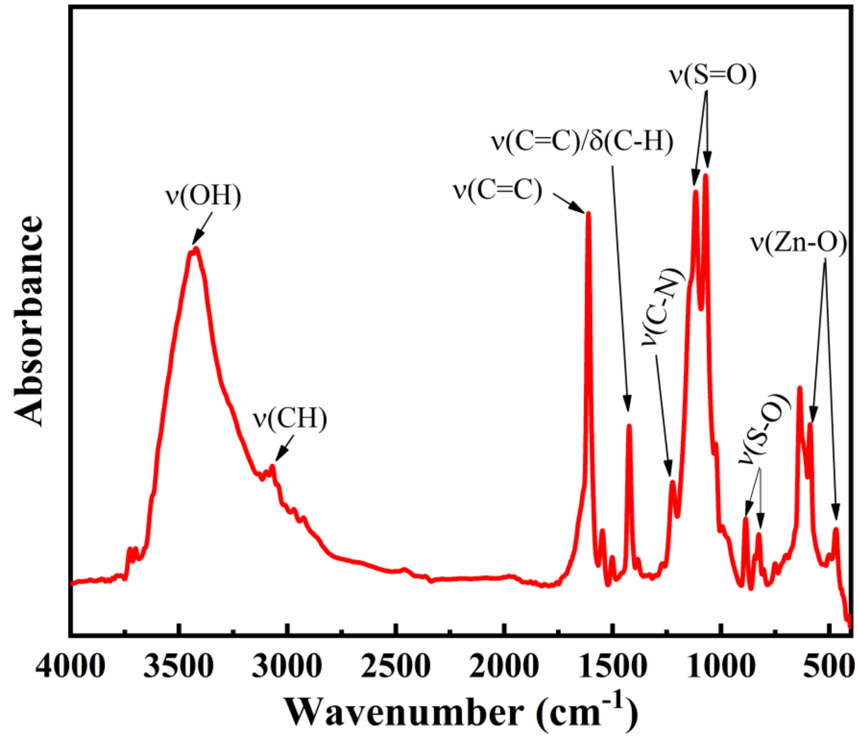

Figure S13. The FT-IR spectrum of the SOFOUR-TEPE-Zn.

The broad peak at 3422.1 cm^{-1} was attributed to the stretching vibration of -OH group due to the water molecules in the framework. The peak at 1611.4 cm^{-1} corresponded to the stretching vibration of C=C bond. The small peaks at 1547.0 and 1501.5 cm^{-1} were attributed to the N-H bending vibration of amide II, and the small peak at 1223.3 cm^{-1} was the N-H bending vibration of amide III. The peak at 1423.6 cm^{-1} belonged to the stretching vibration of C=C or the bending vibration of C-H in the pyridine ring. The strong peaks at 1116.6 and 1071.0 cm^{-1} can be attributed to the antisymmetric stretching vibrations of S=O in SO_4^{2-} groups.[16] The small peaks at 886.3 and 825.8 cm^{-1} belonged to the stretching vibration of S-O. The peaks at 589.3 and 469.3 cm^{-1} corresponded to the Zn-O stretching vibrations.[16-18]

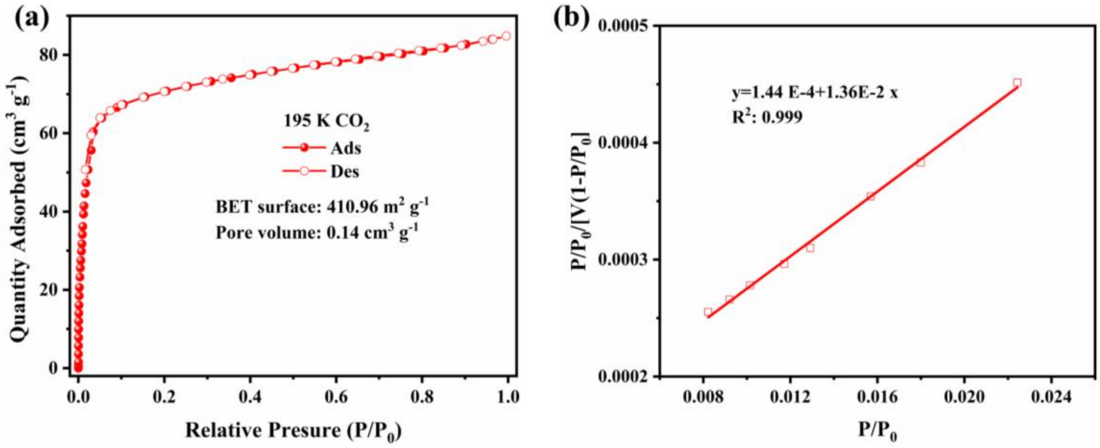

Figure S14. (a) CO_2 adsorption isotherm of SOFOUR-TEPE-Zn at 195 K; (b) BET calculation plot for SOFOUR-TEPE-Zn based on its corresponding CO_2 adsorption isotherm at 195 K.

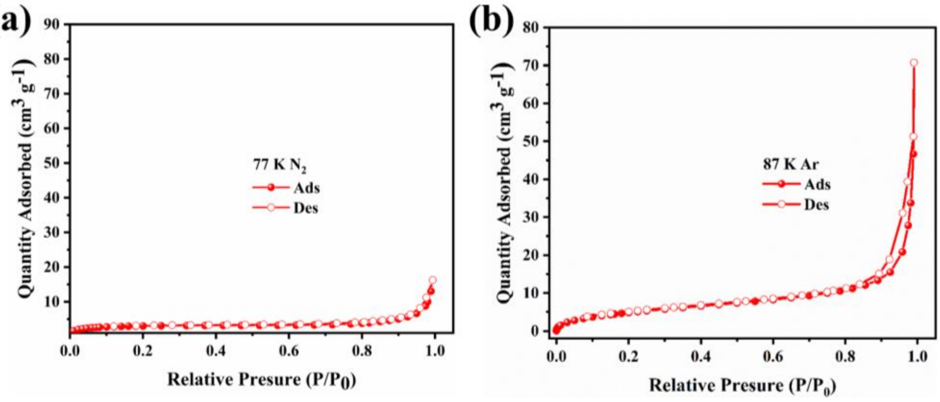

Figure S15. (a) N_2 adsorption isotherm at 77 K and (b) Ar adsorption isotherm at 87 K of SOFOUR-TEPE-Zn.

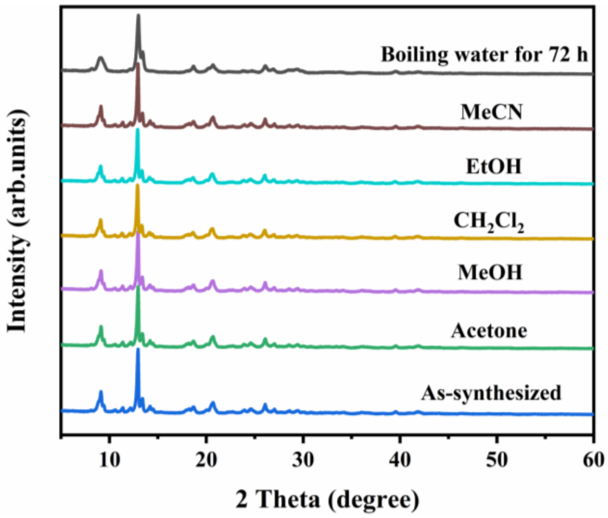

Figure S16. PXRD patterns of SOFOUR-TEPE-Zn after immersing in different solvents for 10 days and boiling water for 72 h.

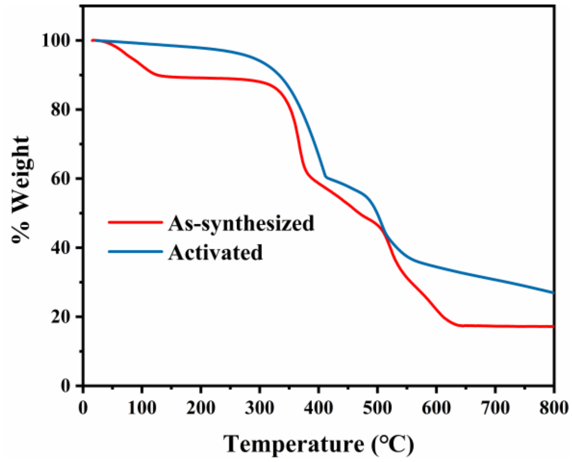

Figure S17. TGA curves of as-synthesized and activated SOFOUR-TEPE-Zn.

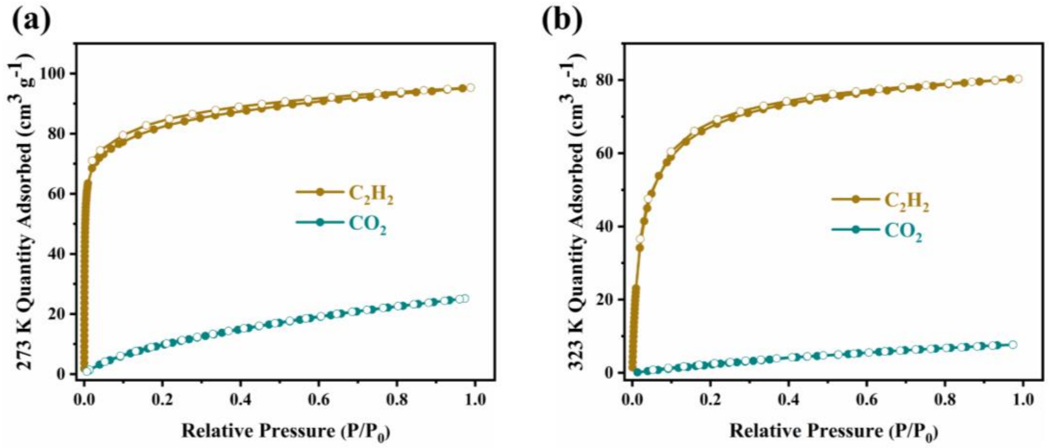

Figure S18. Adsorption isotherms of C_2H_2 and CO_2 on SOFOUR-TEPE-Zn at (a) 273 K and (b) 323 K.

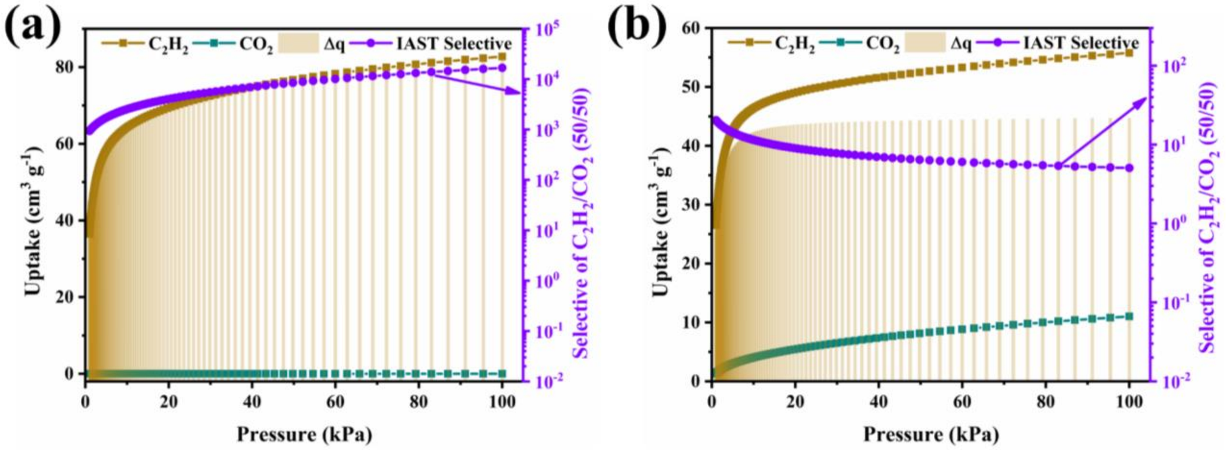

Figure S19. Predicted mixture adsorption isotherms and selectivity of (a) SOFOUR-TEPE-Zn and (b) SOFOUR-1-Zn based on IAST method for a 50:50 C_2H_2/CO_2 mixture at 298 K.

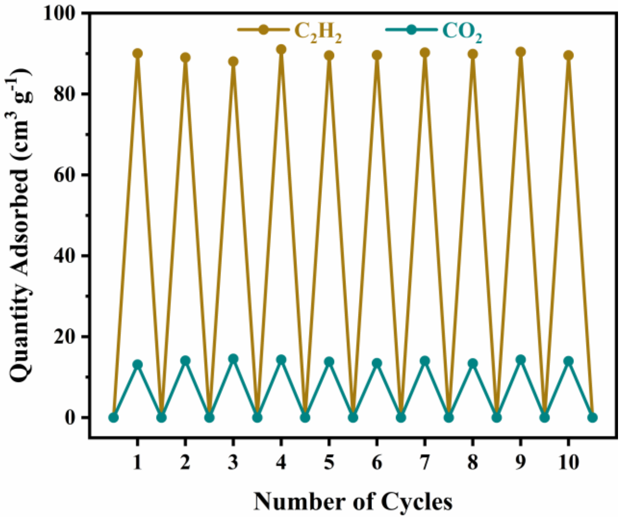

Figure S20. The 10 adsorption cycles of C_2H_2 and CO_2 at 298 K.

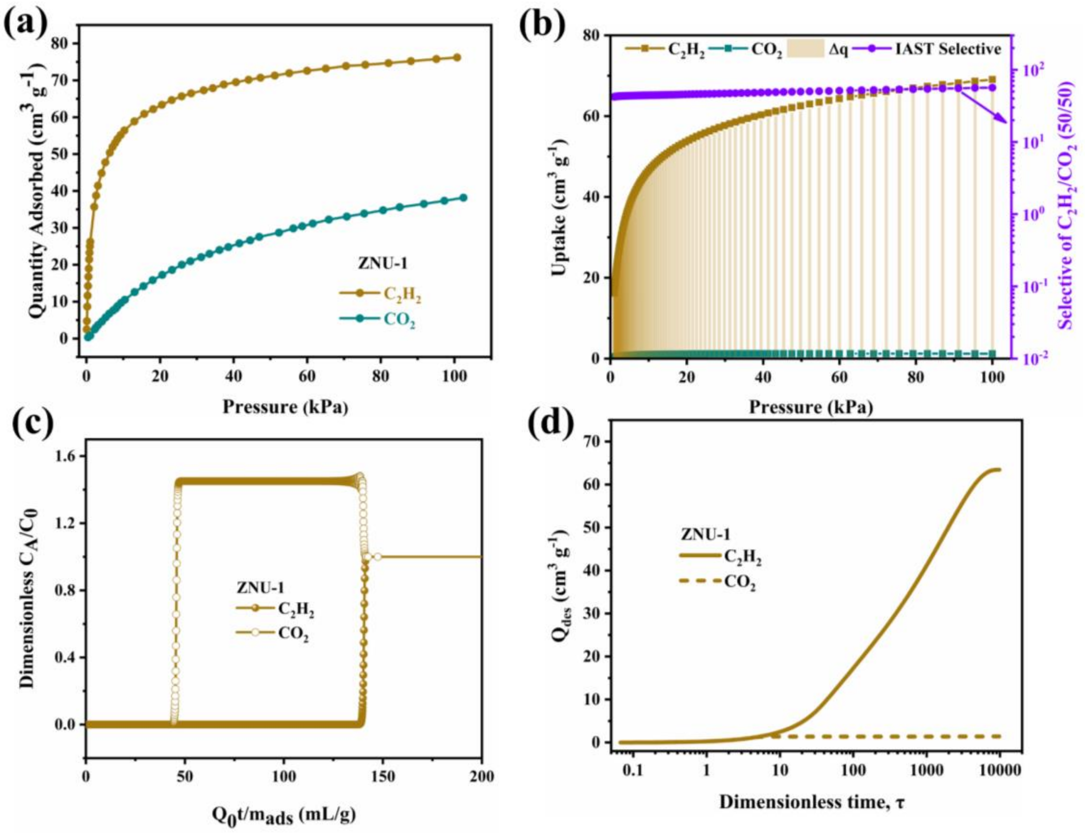

Figure S21. (a) C_2H_2 and CO_2 adsorption isotherms for ZNU-1 at 298 K.[19] (b) Predicted mixture adsorption isotherms and selectivity of ZNU-1 based on IAST method for a 50:50 C_2H_2/CO_2 mixture at 298 K. (c) Simulated breakthrough curve for 50/50 C_2H_2/CO_2 mixtures in fixed bed packed with ZNU-1 operating at 298 K and 100 kPa. (d) Simulations of counter-current blowdown operations for ZNU-1.

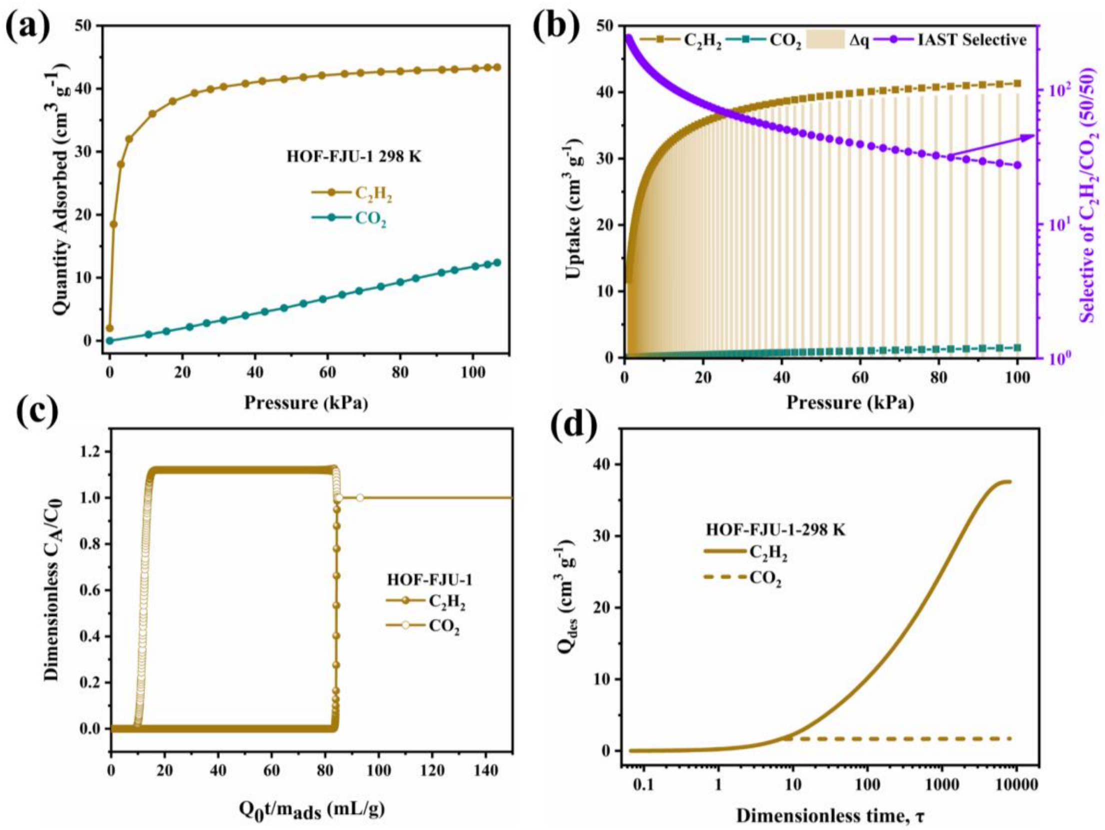

Figure S22. (a) C_2H_2 and CO_2 adsorption isotherms for HOF-FJU-1 at 298 K.[4] (b) Predicted mixture adsorption isotherms and selectivity of HOF-FJU-1 based on IAST method for a 50:50 C_2H_2/CO_2 mixture at 298 K. (c) Simulated breakthrough curve for 50/50 C_2H_2/CO_2 mixtures in fixed bed packed with HOF-FJU-1 operating at 298 K and 100 kPa. (d) Simulations of counter-current blowdown operations for HOF-FJU-1.

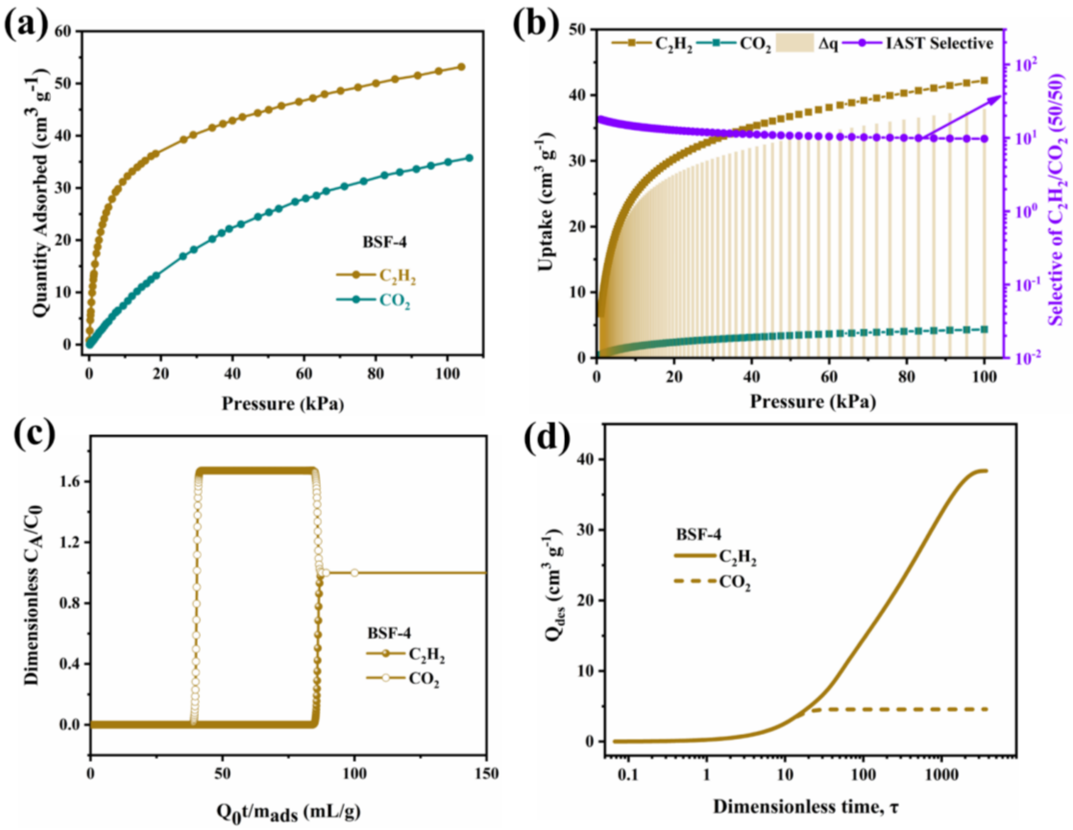

Figure S23. (a) C_2H_2 and CO_2 adsorption isotherms for BSF-4 at 298 K.[19] (b) Predicted mixture adsorption isotherms and selectivity of BSF-4 based on IAST method for a 50:50 C_2H_2/CO_2 mixture at 298 K. (c) Simulated breakthrough curve for 50/50 C_2H_2/CO_2 mixtures in fixed bed packed with BSF-4 operating at 298 K and 100 kPa. (d) Simulations of counter-current blowdown operations for BSF-4.

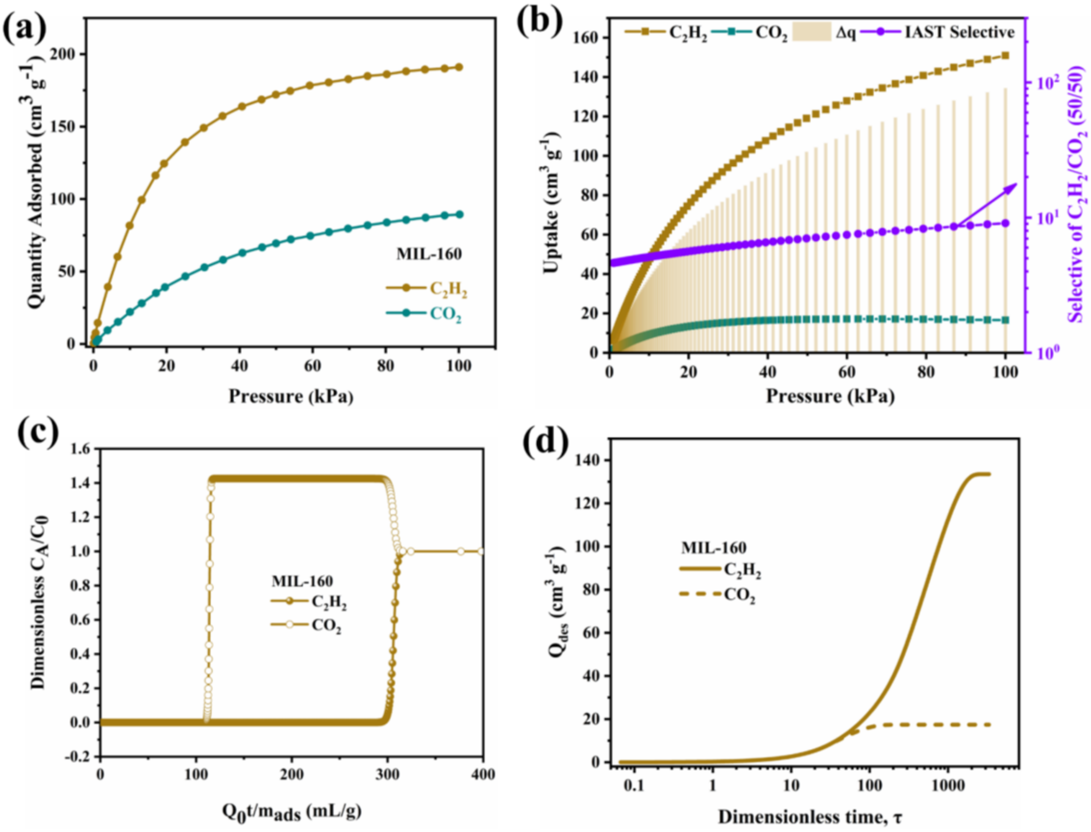

Figure S24. (a) C_2H_2 and CO_2 adsorption isotherms for MIL-160 at 298 K.[20] (b) Predicted mixture adsorption isotherms and selectivity of MIL-160 based on IAST method for a 50:50 C_2H_2/CO_2 mixture at 298 K. (c) Simulated breakthrough curve for 50/50 C_2H_2/CO_2 mixtures in fixed bed packed with MIL-160 operating at 298 K and 100 kPa. (d) Simulations of counter-current blowdown operations for MIL-160.

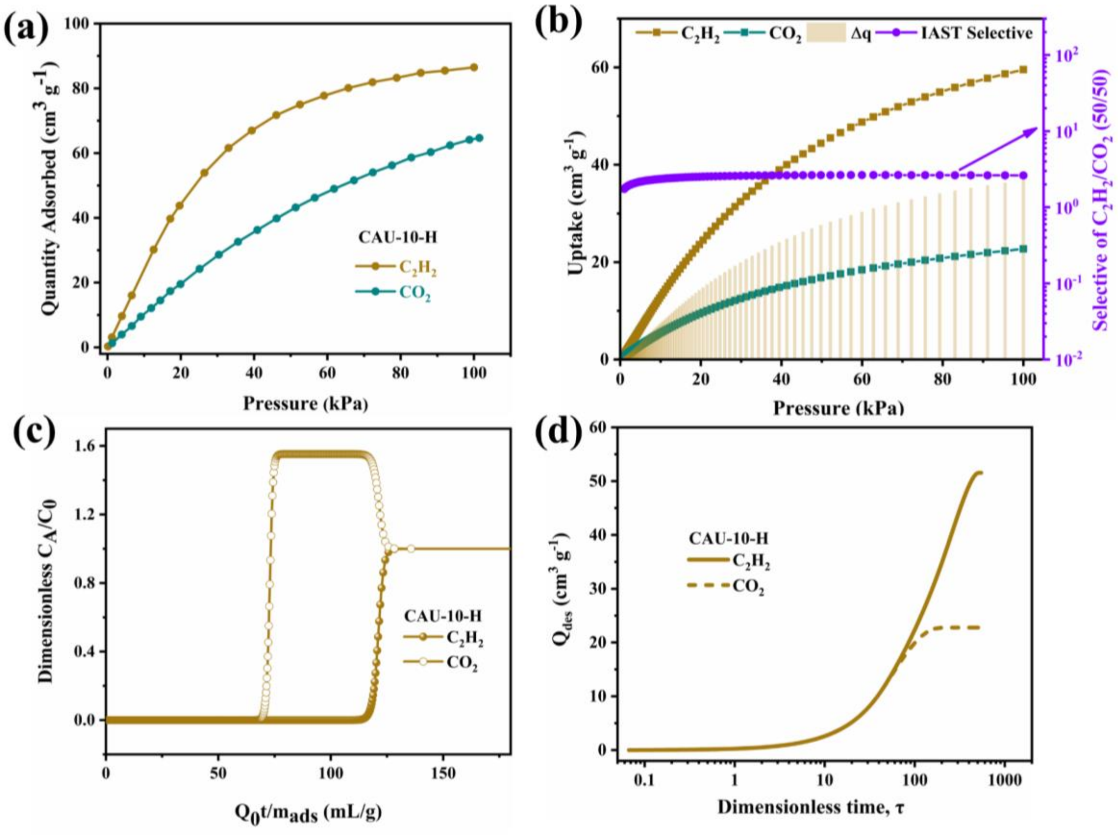

Figure S25. (a) C_2H_2 and CO_2 adsorption isotherms for CAU-10-H at 298 K.[21] (b) Predicted mixture adsorption isotherms and selectivity of CAU-10-H based on IAST method for a 50:50 C_2H_2/CO_2 mixture at 298 K. (c) Simulated breakthrough curve for 50/50 C_2H_2/CO_2 mixtures in fixed bed packed with CAU-10-H operating at 298 K and 100 kPa. (d) Simulations of counter-current blowdown operations for CAU-10-H.

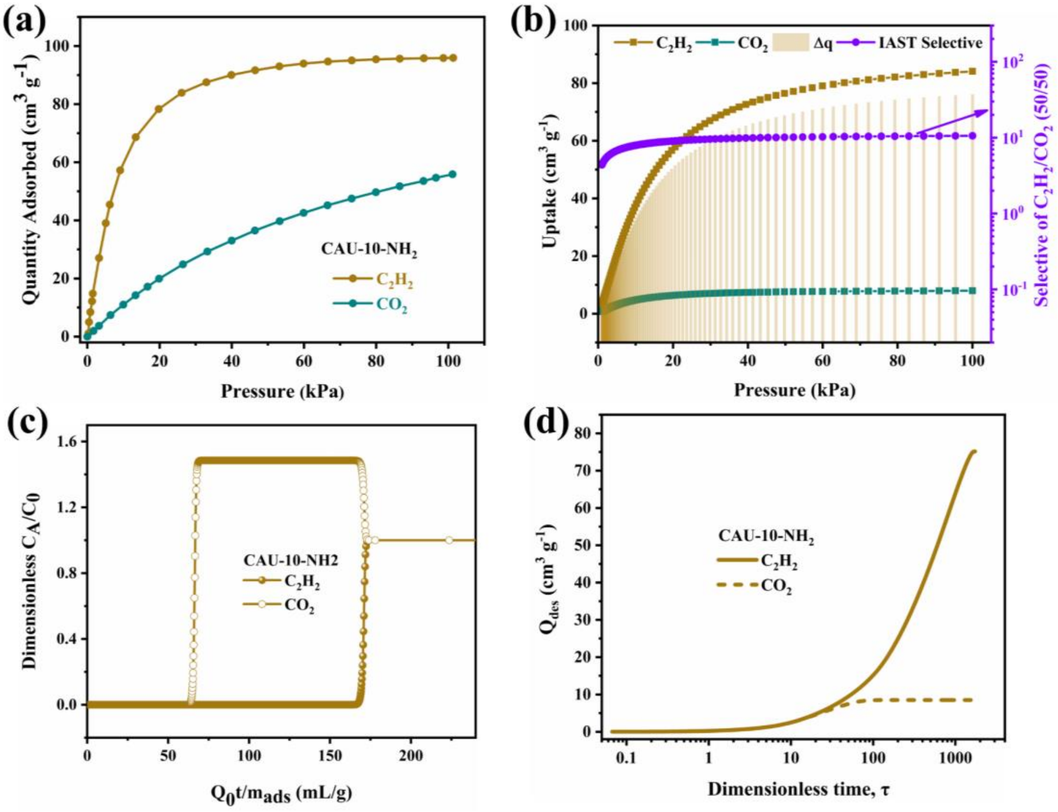

Figure S26. (a) C_2H_2 and CO_2 adsorption isotherms for CAU-10-NH_2 at 298 K.[22] (b) Predicted mixture adsorption isotherms and selectivity of CAU-10-NH_2 based on IAST method for a 50:50 C_2H_2/CO_2 mixture at 298 K. (c) Simulated breakthrough curve for 50/50 C_2H_2/CO_2 mixtures in fixed bed packed with CAU-10-NH_2 operating at 298 K and 100 kPa. (d) Simulations of counter-current blowdown operations for CAU-10-NH_2.

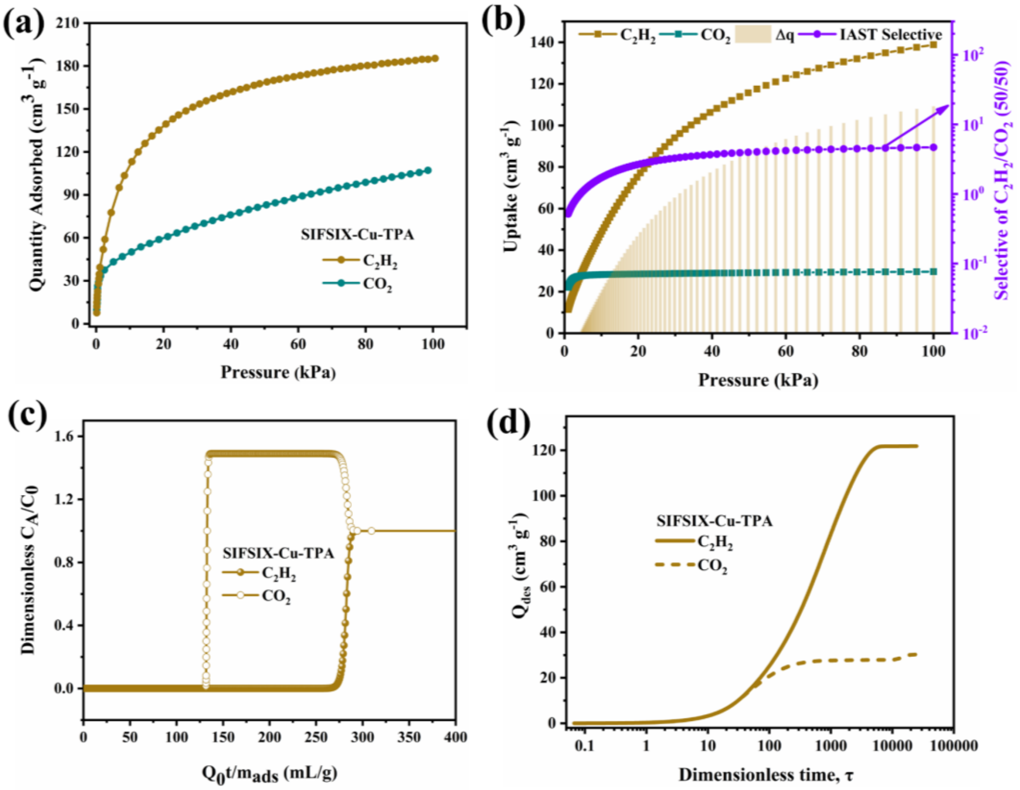

Figure S27. (a) C_2H_2 and CO_2 adsorption isotherms for SIFSIX-Cu-TPA at 298 K.[23] (b) Predicted mixture adsorption isotherms and selectivity of SIFSIX-Cu-TPA based on IAST method for a 50:50 C_2H_2/CO_2 mixture at 298 K. (c) Simulated breakthrough curve for 50/50 C_2H_2/CO_2 mixtures in fixed bed packed with SIFSIX-Cu-TPA operating at 298 K and 100 kPa. (d) Simulations of counter-current blowdown operations for SIFSIX-Cu-TPA.

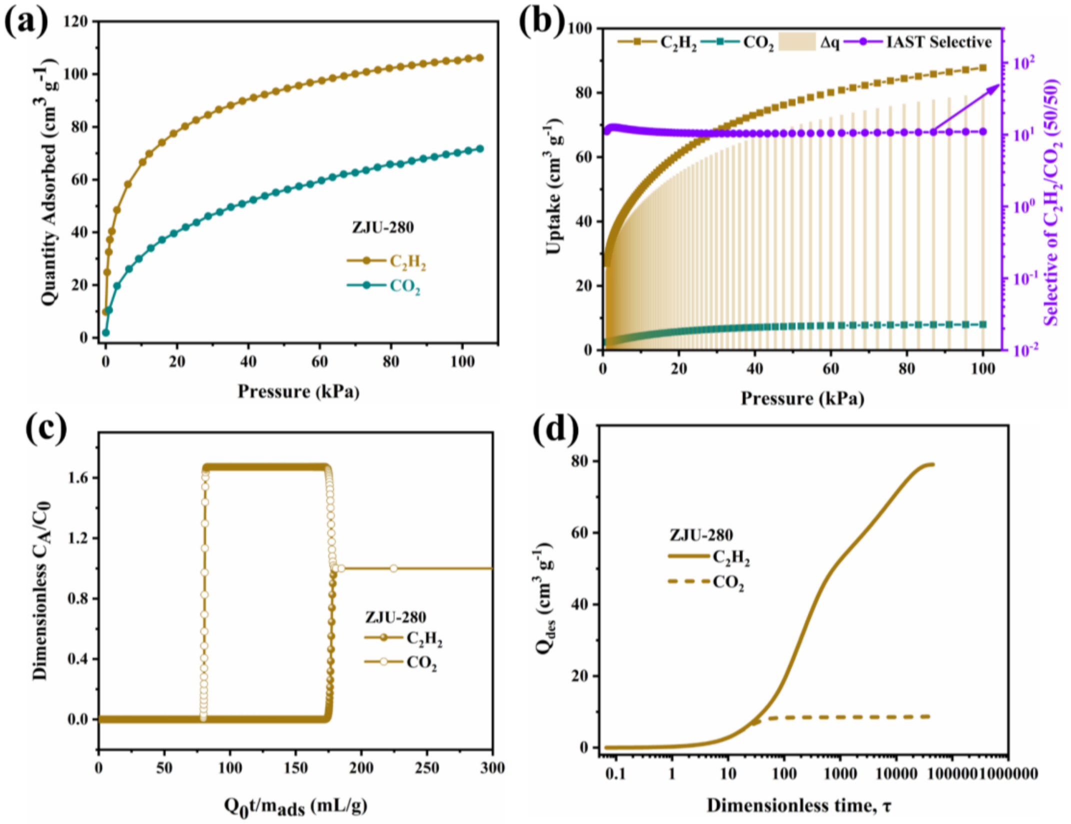

Figure S28. (a) C_2H_2 and CO_2 adsorption isotherms for ZJU-280 at 298 K.[24] (b) Predicted mixture adsorption isotherms and selectivity of ZJU-280 based on IAST method for a 50:50 C_2H_2/CO_2 mixture at 298 K. (c) Simulated breakthrough curve for 50/50 C_2H_2/CO_2 mixtures in fixed bed packed with ZJU-280 operating at 298 K and 100 kPa. (d) Simulations of counter-current blowdown operations for ZJU-280.

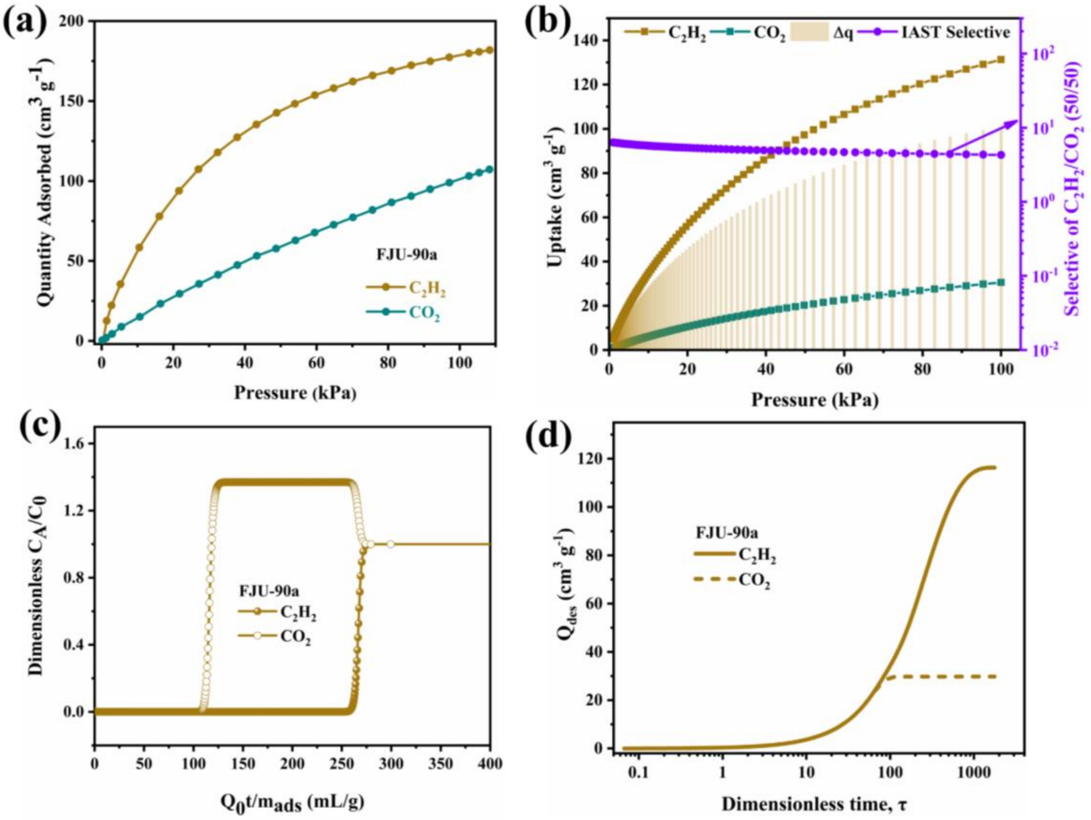

Figure S29. (a) C_2H_2 and CO_2 adsorption isotherms for FJU-90a at 298 K.[25] (b) Predicted mixture adsorption isotherms and selectivity of FJU-90a based on IAST method for a 50:50 C_2H_2/CO_2 mixture at 298 K. (c) Simulated breakthrough curve for 50/50 C_2H_2/CO_2 mixtures in fixed bed packed with FJU-90a operating at 298 K and 100 kPa. (d) Simulations of counter-current blowdown operations for FJU-90a.

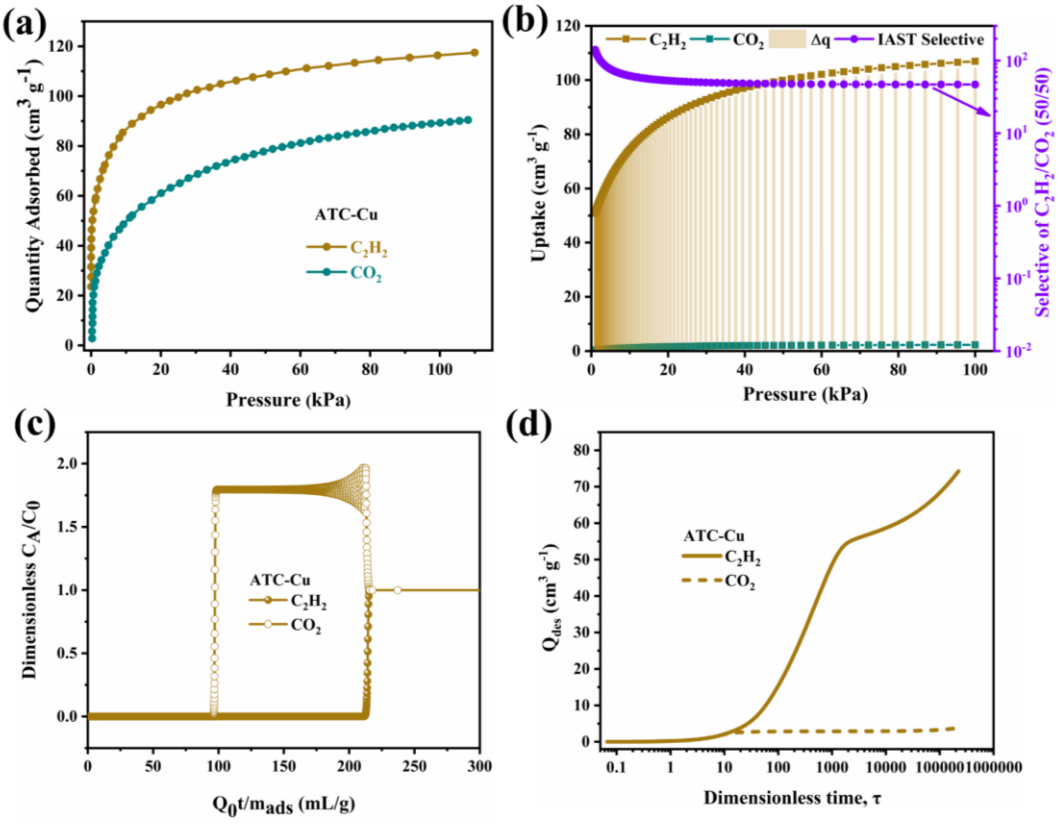

Figure S30. (a) C_2H_2 and CO_2 adsorption isotherms for ATC-Cu at 298 K.[26] (b) Predicted mixture adsorption isotherms and selectivity of ATC-Cu based on IAST method for a 50:50 C_2H_2/CO_2 mixture at 298 K. (c) Simulated breakthrough curve for 50/50 C_2H_2/CO_2 mixtures in fixed bed packed with ATC-Cu operating at 298 K and 100 kPa. (d) Simulations of counter-current blowdown operations for ATC-Cu.

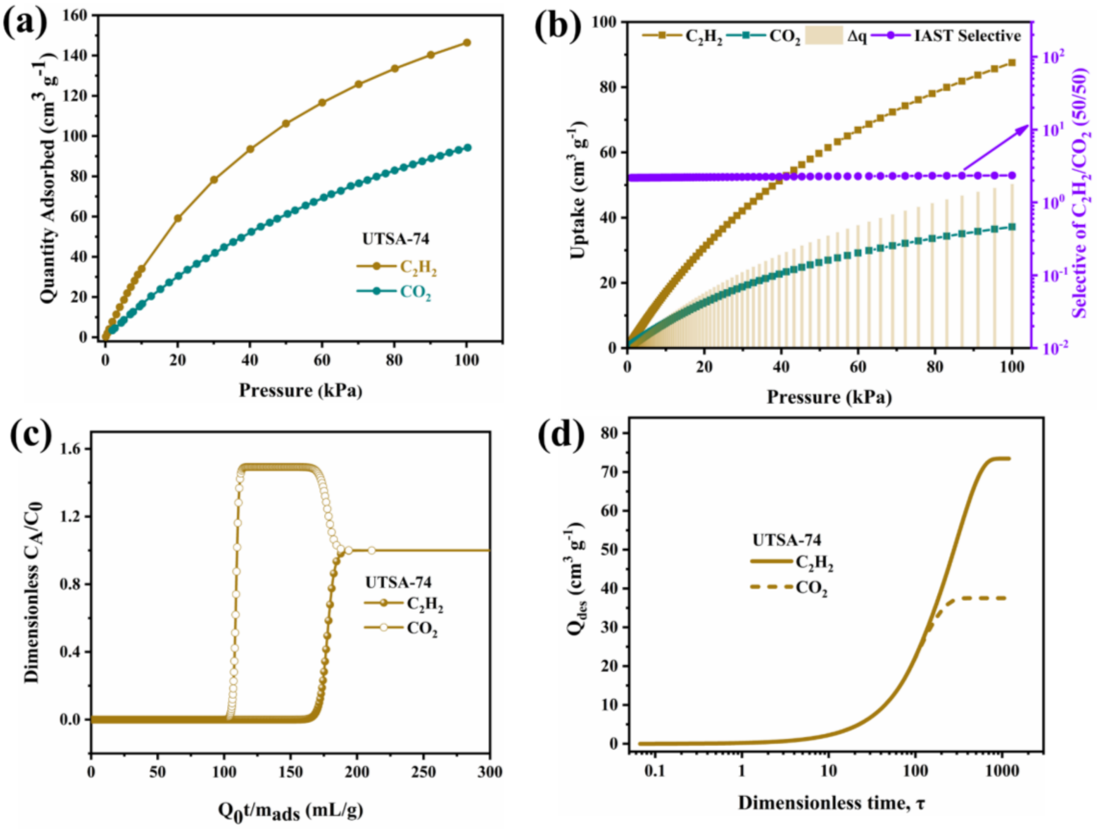

Figure S31. (a) C_2H_2 and CO_2 adsorption isotherms for UTSA-74 at 298 K.[27] (b) Predicted mixture adsorption isotherms and selectivity of UTSA-74 based on IAST method for a 50:50 C_2H_2/CO_2 mixture at 298 K. (c) Simulated breakthrough curve for 50/50 C_2H_2/CO_2 mixtures in fixed bed packed with UTSA-74 operating at 298 K and 100 kPa. (d) Simulations of counter-current blowdown operations for UTSA-74.

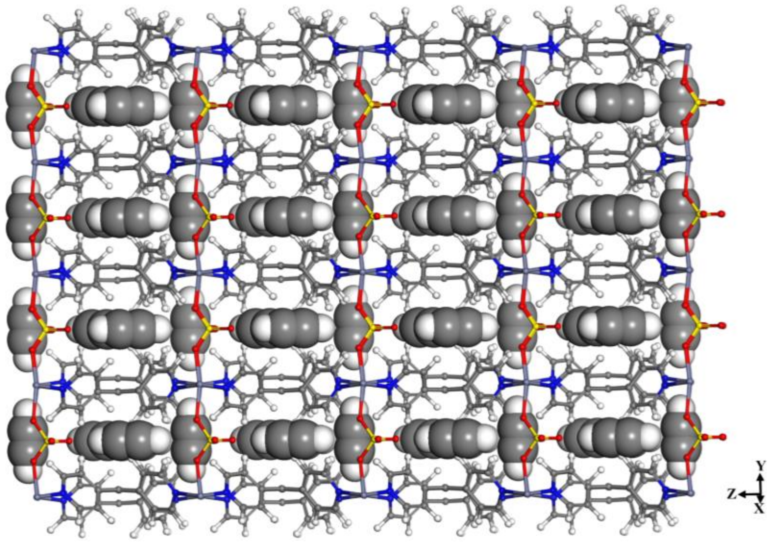

Figure S32. Dense packing of C_2H_2 molecules in SOFOUR-TEPE-Zn.

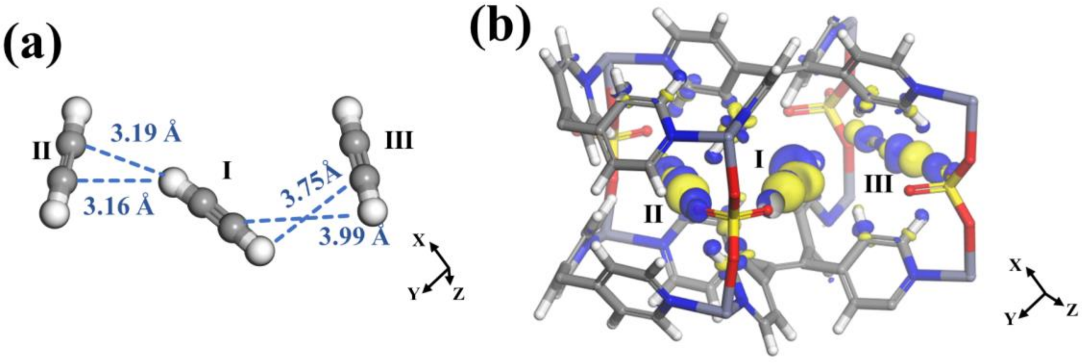

Figure S33. (a) Guest-guest interactions between C_2H_2 molecules; (b) Charge density difference plots showing the interactions between framework and C_2H_2 (Sites I-III).

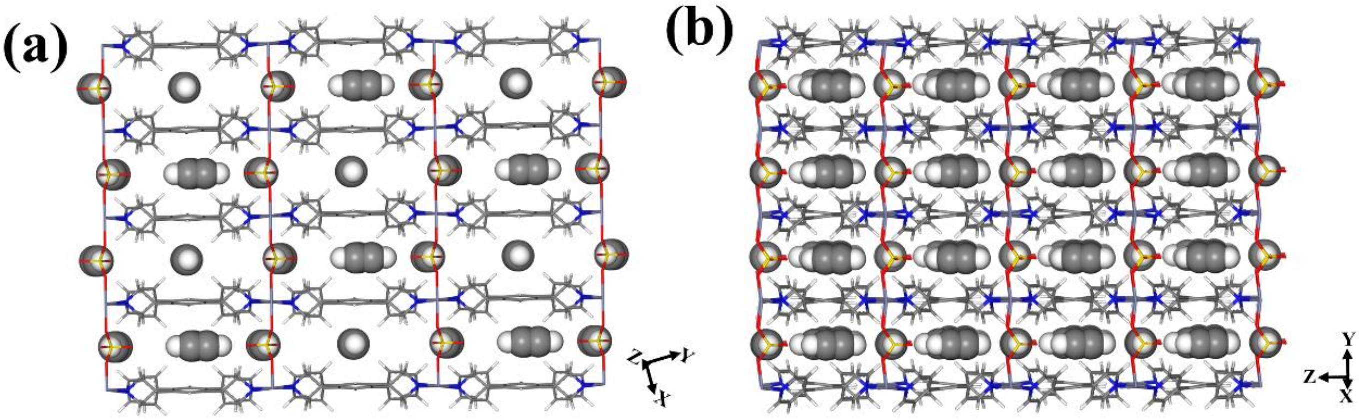

Figure S34. The packing pattern of C_2H_2 molecules in SOFOUR-1-Zn: (a) viewed along the *Z-axes* and (b) viewed along the *X-axes.*

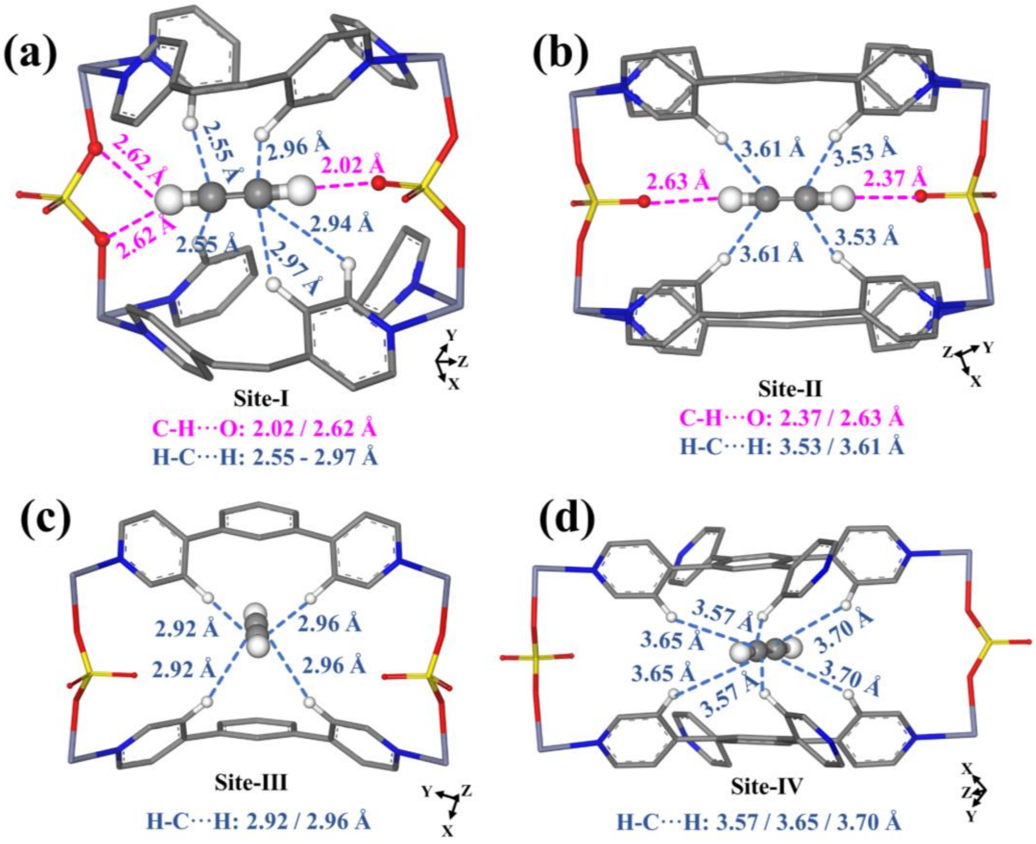

Figure S35. C_2H_2 binding sites in SOFOUR-1-Zn by DFT calculations.

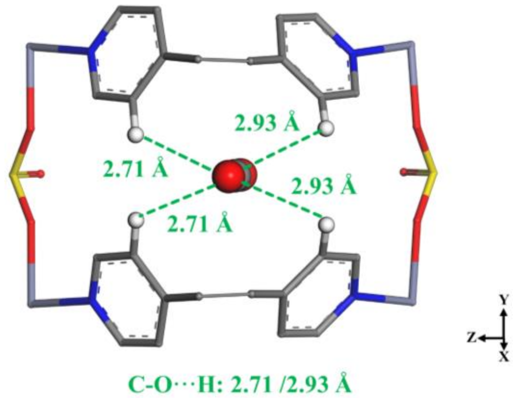

Figure S36. DFT-derived CO_2 binding site in SOFOUR-TEPE-Zn (△E = -33.38 kJ mol^{-1}**)**

.

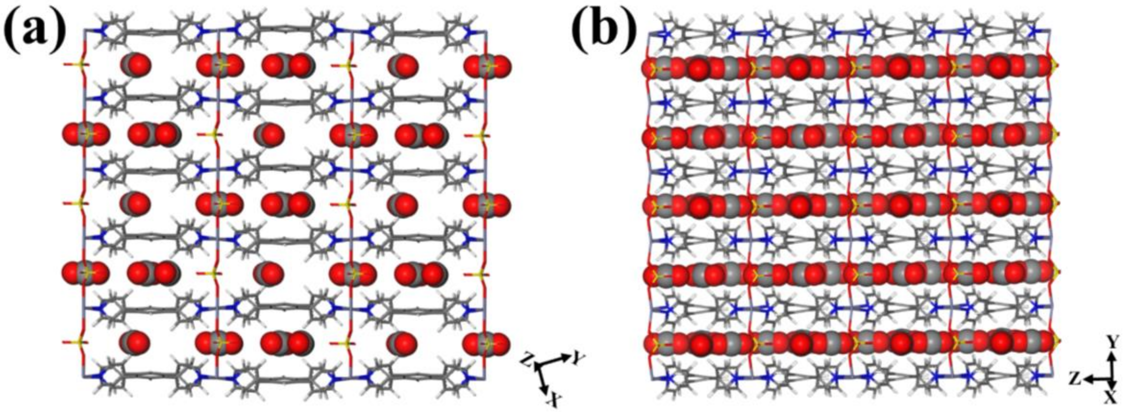

Figure S37. The packing pattern of CO_2 molecules in SOFOUR-1-Zn: (a) viewed along the *Z-axes* and (b) viewed along the *X-axes.*

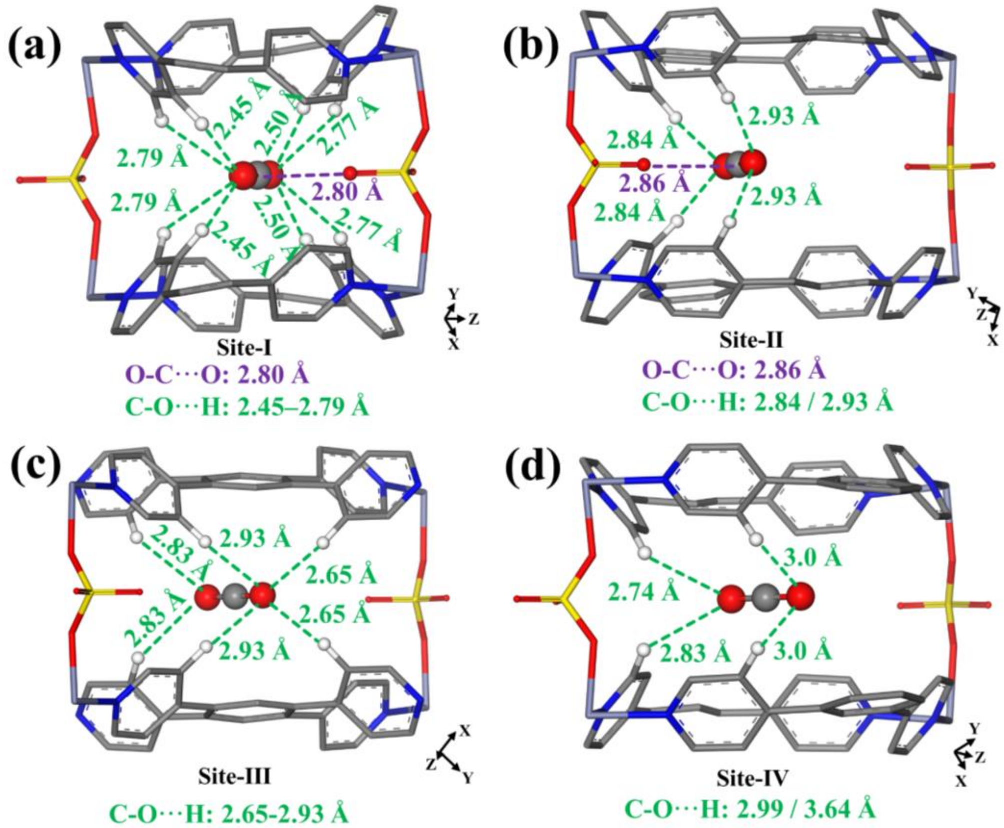

Figure S38. CO_2 binding sites in SOFOUR-1-Zn by DFT calculations.

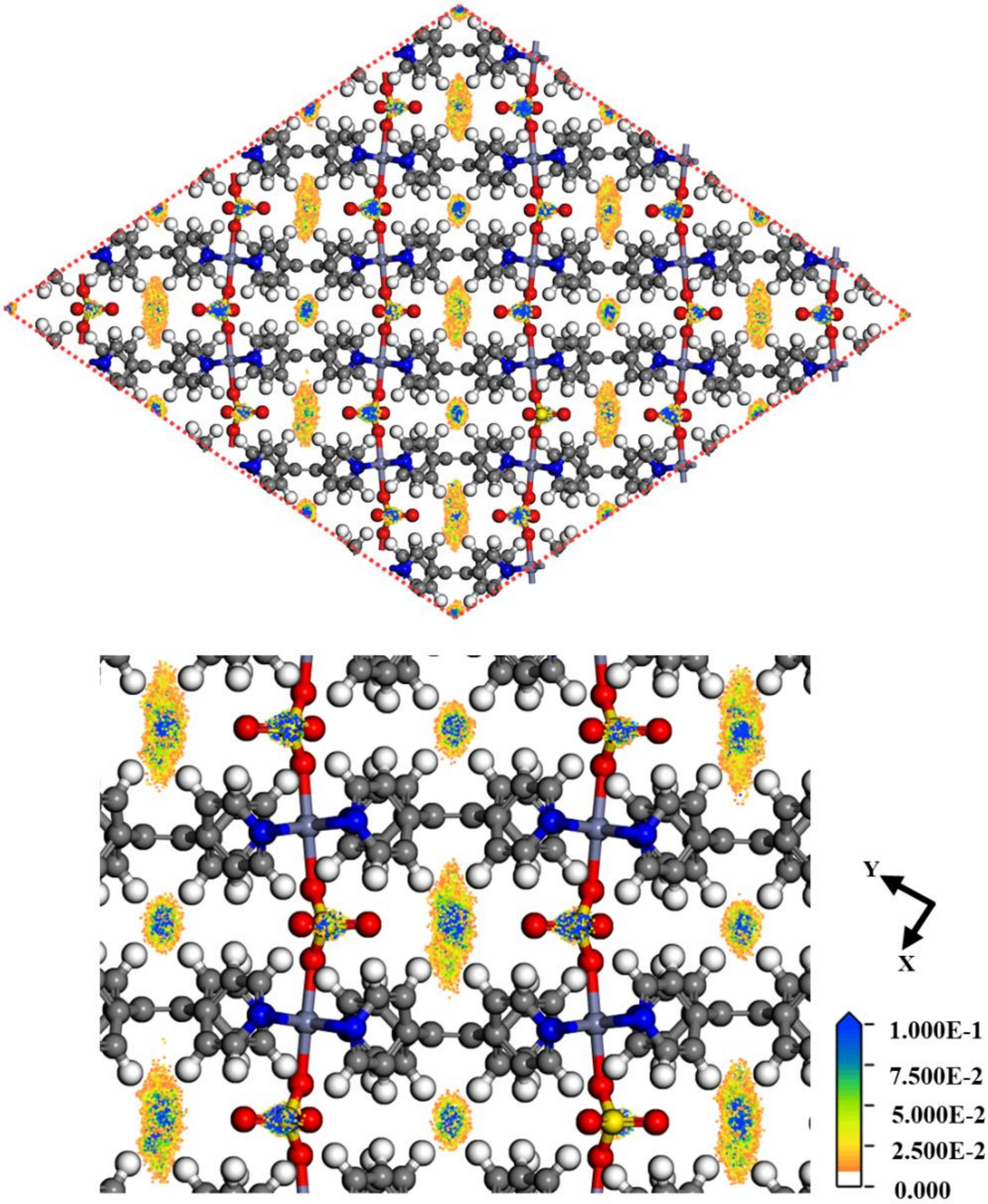

Figure S39. GCMC simulations for the distribution density of C_2H_2 in SOFOUR-TEPE-Zn at 1 kPa.

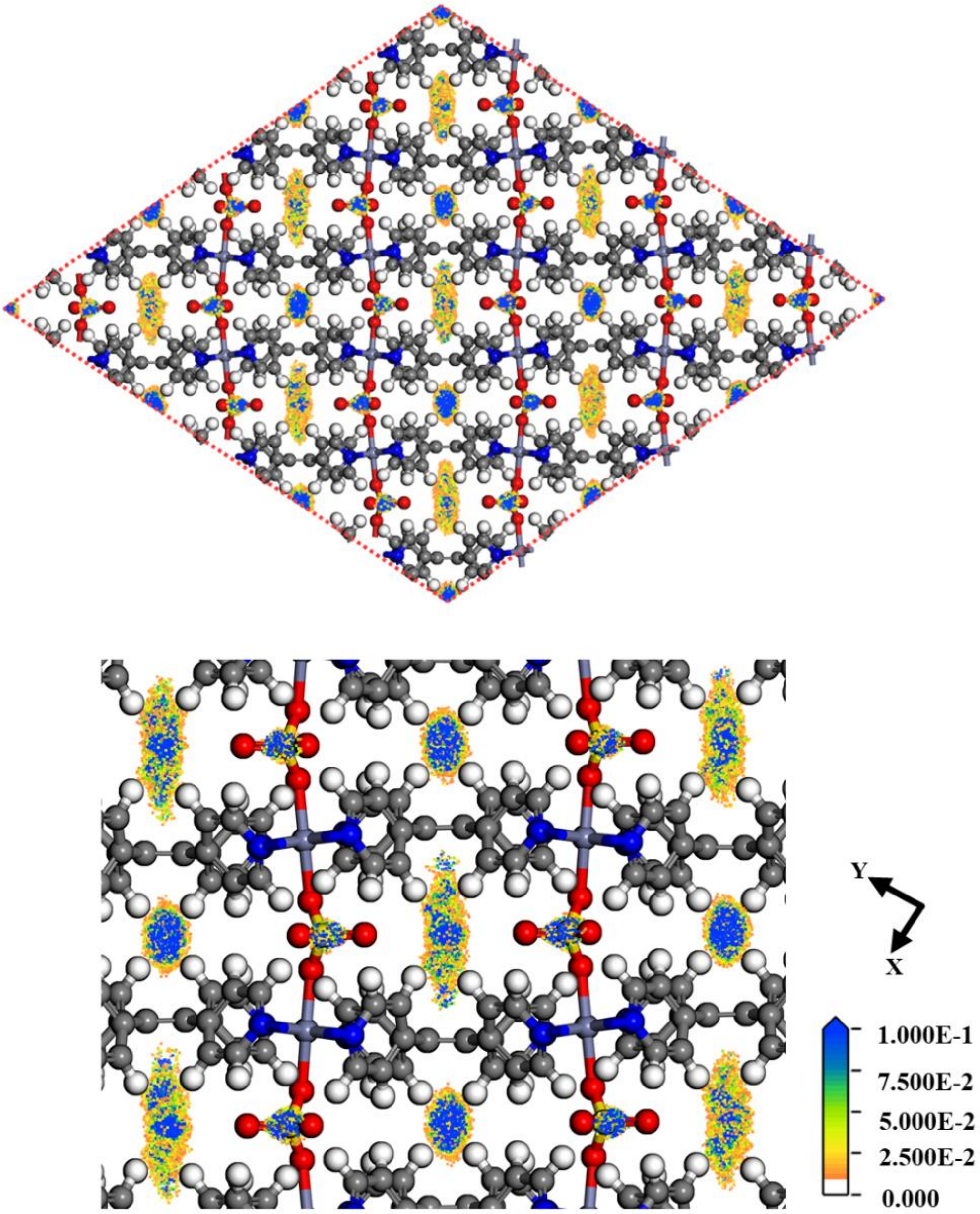

Figure S40. GCMC simulations for the distribution density of C_2H_2 in SOFOUR-TEPE-Zn at 50 kPa.

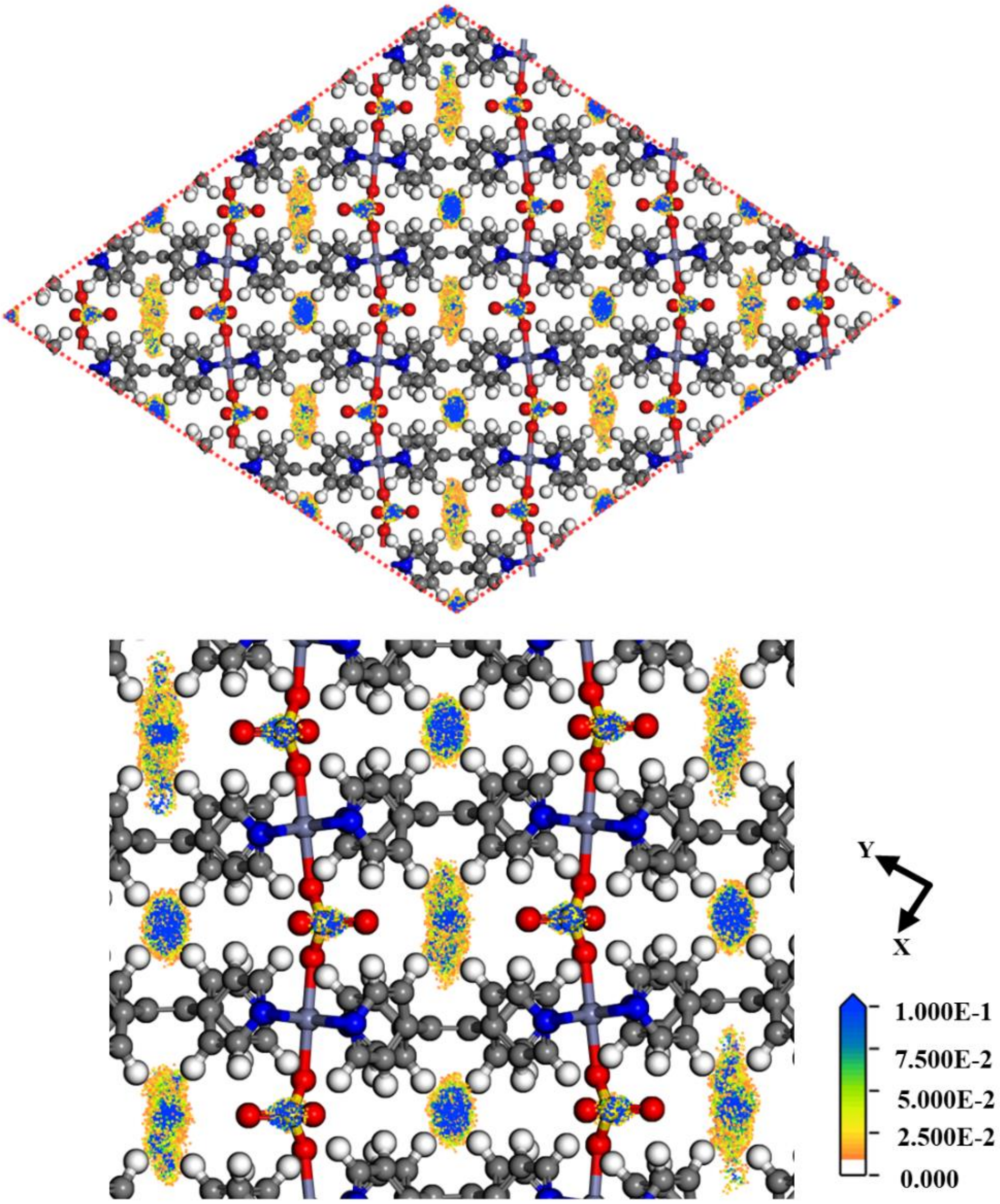

Figure S41. GCMC simulations for the distribution density of C_2H_2 in SOFOUR-TEPE-Zn at 100 kPa.

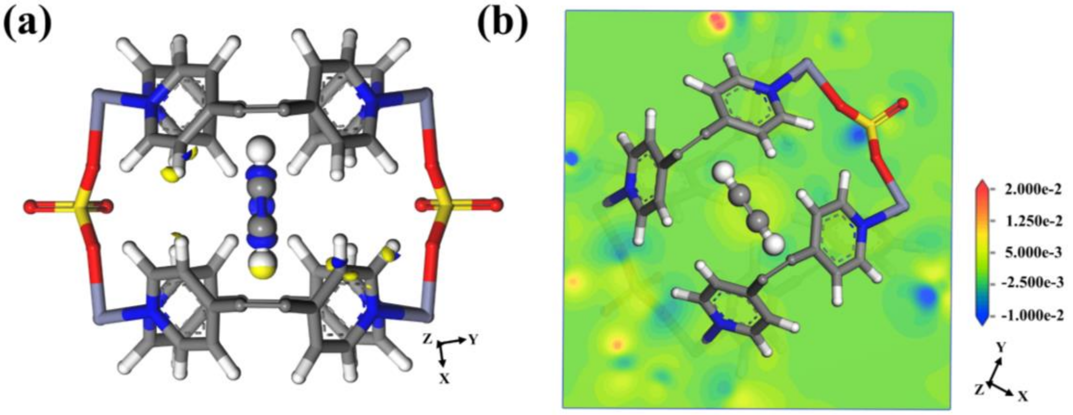

Figure S42. Charge density difference plots showing the interaction between framework and C_2H_2 (Site IV).

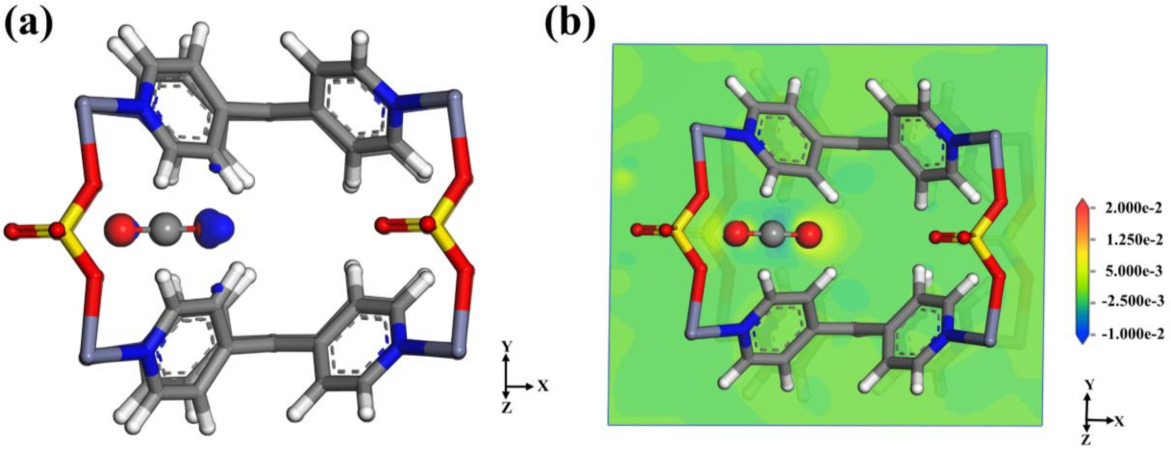

Figure S43. Charge density difference plots showing the interaction between framework and CO_2.

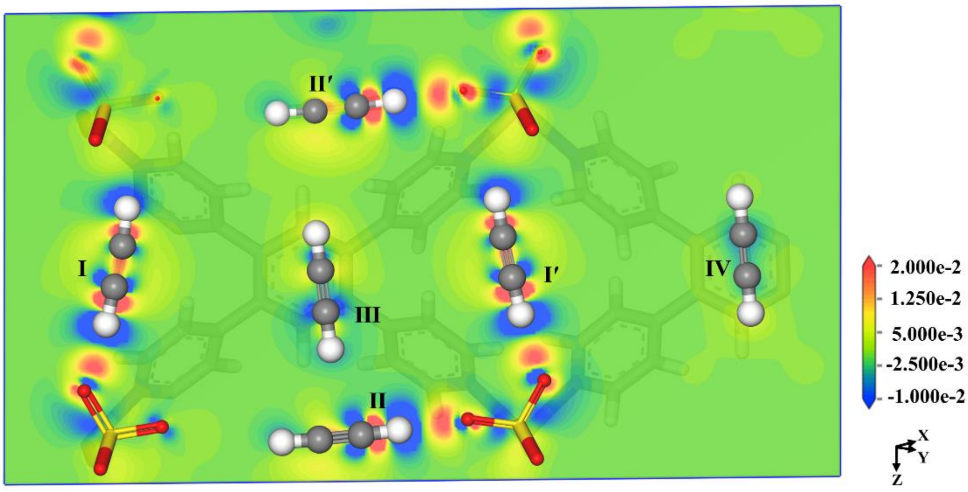

Figure S44. Charge density difference plots of C_2H_2-loaded in SOFOUR-1-Zn.

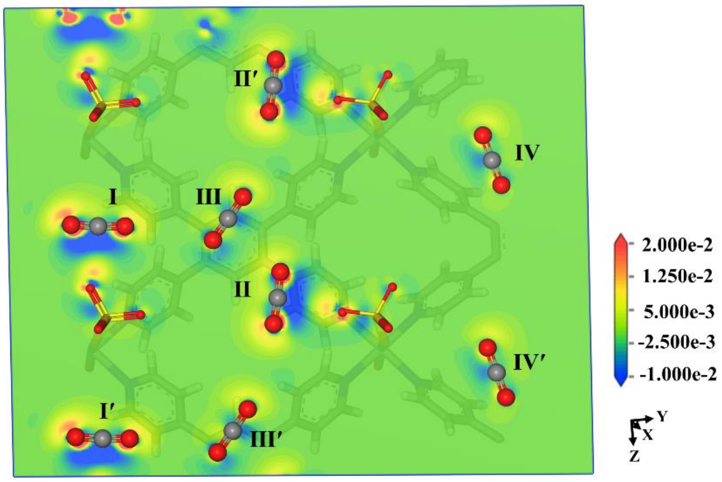

Figure S45. Charge density difference plots of CO_2-loaded in SOFOUR-1-Zn.

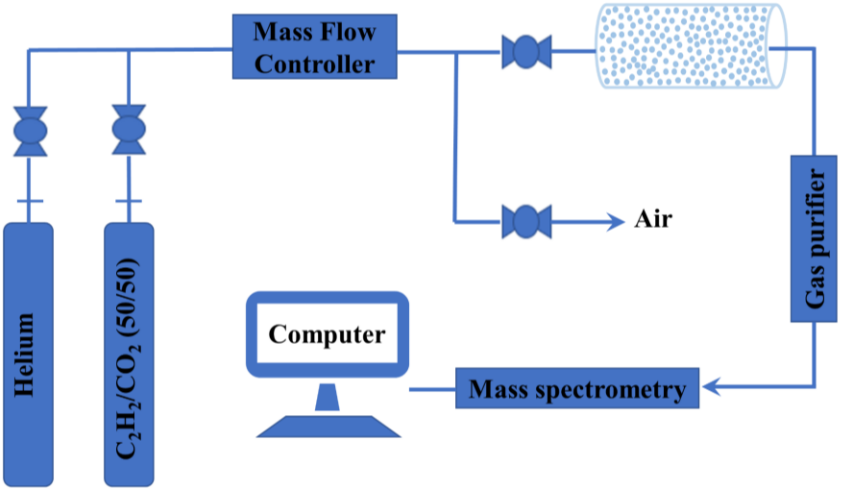

Figure S46. Breakthrough experiments apparatus.

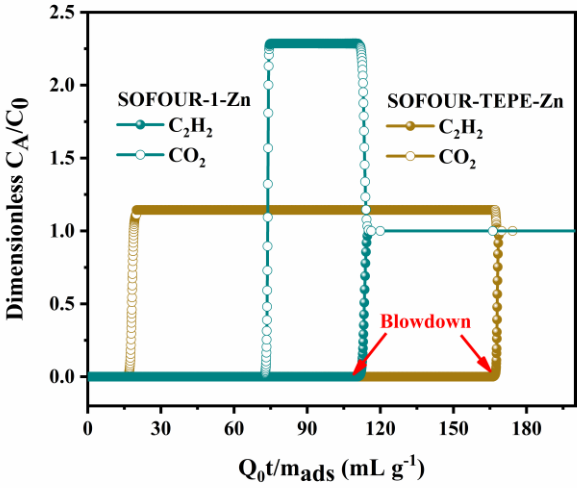

Figure S47. Simulated breakthrough curves for 50/50 C_2H_2/CO_2 mixtures in fixed bed packed with SOFOUR-TEPE-Zn and SOFOUR-1-Zn operating at 298 K and 100 kPa.

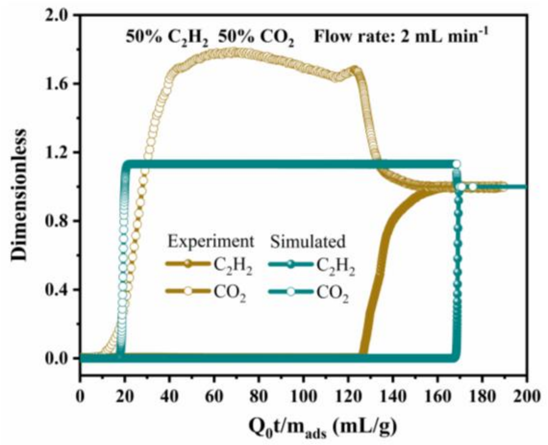

Figure S48. Comparison of experimental and simulated breakthrough curves for 50/50 C_2H_2/CO_2 mixtures in fixed bed packed with SOFOUR-TEPE-Zn operating at 298 K and 100 kPa. The flow rate at the inlet is 2.0 mL min^{-1}.

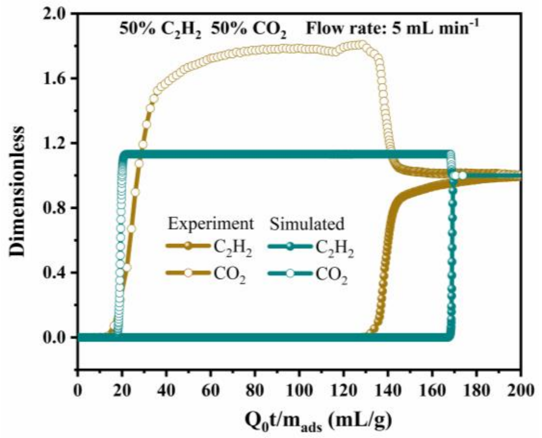

Figure S49. Comparison of experimental and simulated breakthrough curves for 50/50 C_2H_2/CO_2 mixtures in fixed bed packed with SOFOUR-TEPE-Zn operating at 298 K and 100 kPa. The flow rate at the inlet is 5.0 mL min^{-1}.

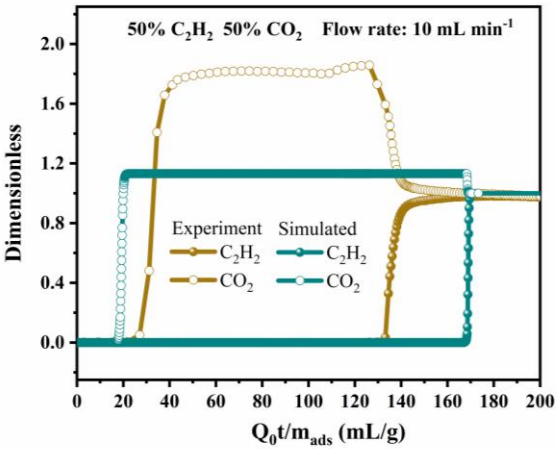

Figure S50. Comparison of experimental and simulated breakthrough curves for 50/50 C_2H_2/CO_2 mixtures in fixed bed packed with SOFOUR-TEPE-Zn operating at 298 K and 100 kPa. The flow rate at the inlet is 10.0 mL min^{-1}.

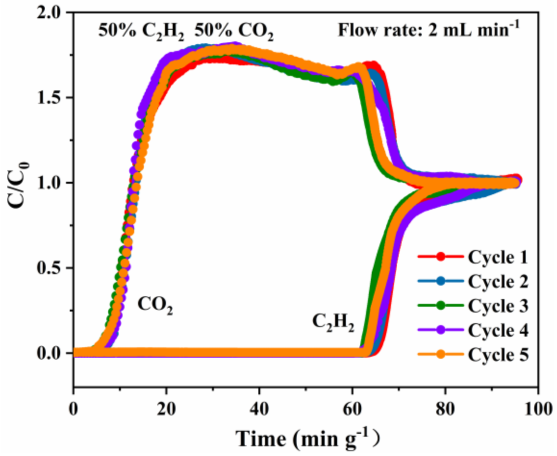

Figure S51. Cycling breakthrough tests for C_2H_2/CO_2 (50/50, *v/v*) on SOFOUR-TEPE-Zn at room temperature (flow rate: 2.0 mL min^{-1}).

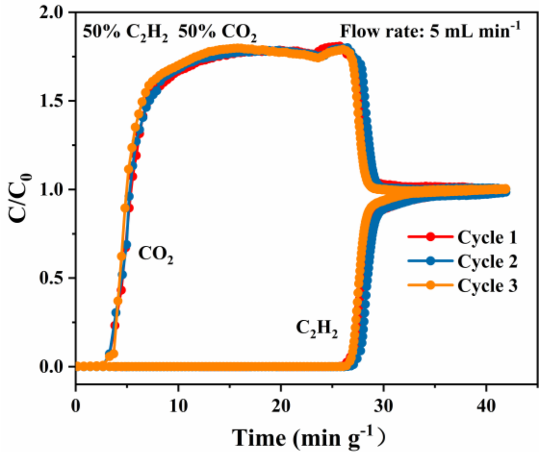

Figure S52. Cycling breakthrough tests for C_2H_2/CO_2 (50/50, *v/v*) on SOFOUR-TEPE-Zn at room temperature (flow rate: 5.0 mL min^{-1}).

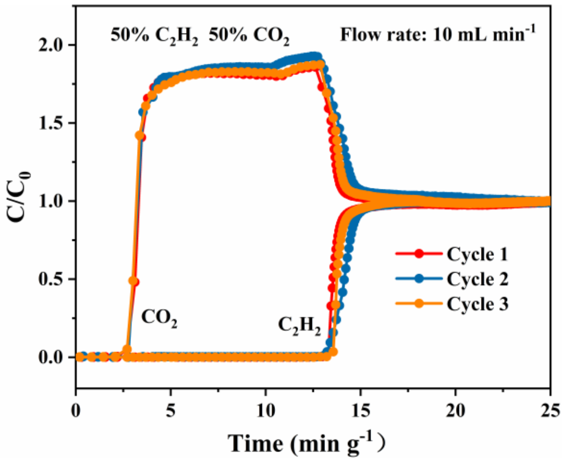

Figure S53. Cycling breakthrough tests for C_2H_2/CO_2 (50/50, *v/v*) on SOFOUR-TEPE-Zn at room temperature (flow rate: 10.0 mL min^{-1}).

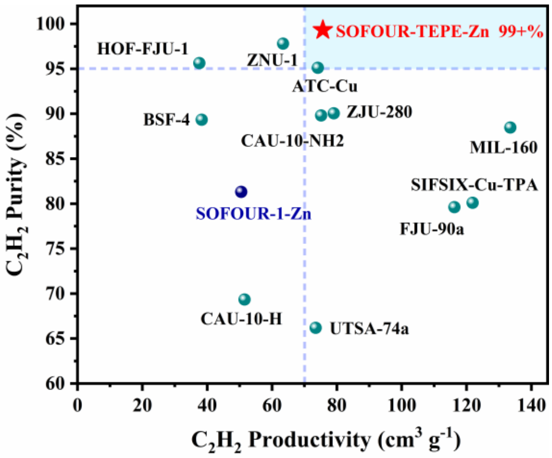

Figure S54. Comparison of the C_2H_2 productivity and purity with 100% C_2H_2 recovery during counter-current blowdown process.

Table S1. Lattice parameters of the modeled structure of SOFOUR-TEPE-Zn and SOFOUR-1-Zn[28].

Unit cell parameters	SOFOUR-TEPE-Zn	SOFOUR-1-Zn
Formula	$C_{22}H_{16}N_4O_4SZn$	$C_{26}H_{18}N_4O_4SZn$
Formula weight	497.858	547.87
Crystal system	Orthorhombic	Orthorhombic
Space group	*Cmm2*	*Cmm2*
a (Å)	13.15101	13.0325
b (Å)	19.41220	25.0760
c (Å)	9.63340	9.4686
α (°)	90.000	90.000
β (°)	90.000	90.000
γ (°)	90.000	90.000
V (Å^3)	2459.31	3094.37
Z	4.000	4
D_{calcd} (g cm^{-3})	1.34556	1.176
$R_p{}^a$	0.04272	/
$R_{wp}{}^b$	0.05574	/

Table S2. Unit cell parameters and reliability of fitting for SOFOUR-TEPE-Zn.

Parameters	**Initial**	**Final**
a	12.9776	13.15101
b	20.02782	19.41220
c	9.1038	9.6334
α	90.000	90.000
β	90.00	90.00
γ	90.000	90.000
R_p = 4.272%, R_{wp} = 5.574%, GOF= 2.194, R_f = 2.157%, R_b = 1.453%		

Table S3. List of atomic coordinates for the modeled structure of SOFOUR-TEPE-Zn.

Atom	x/a	y/b	z/c	B	Site
O1	0.39084	0.75390	0.94538	2.606	1
N2	0.25181	0.67873	0.76486	2.229	1
N3	0.26028	0.67552	0.06341	1.960	1
C4	0.18575	0.68269	0.65581	2.413	1
C5	0.18214	0.63221	0.55204	2.658	1
C6	0.25502	0.57969	0.54696	2.498	1
C7	0.33126	0.58196	0.64998	2.552	1
C8	0.32421	0.62839	0.76275	2.560	1
C9	0.26438	0.57788	0.28414	2.089	1
C10	0.18253	0.58161	0.19003	3.098	1
C11	0.18511	0.62720	0.07594	2.673	1
C12	0.33580	0.67657	0.16240	2.703	1
C13	0.34122	0.62701	0.26813	2.861	1
C14	0.26113	0.53581	0.41670	0.000	1
H15	0.13691	0.72634	0.64515	2.896	1
H16	0.12591	0.63698	0.47052	3.190	1
H17	0.40019	0.55303	0.63904	3.062	1
H18	0.38180	0.62757	0.84311	3.072	1
H19	0.11339	0.55367	0.20884	3.718	1
H20	0.12279	0.62656	0.00231	3.207	1
H21	0.39187	0.71715	0.16551	3.244	1
H22	0.40206	0.63010	0.34362	3.433	1
Zn23	0.25000	0.75000	0.91588	1.778	1
S24	0.50000	0.76379	0.84670	2.039	1
O25	0.50000	0.83698	0.78414	2.744	1
O26	0.50000	0.71317	0.72304	2.785	1

Table S4. Ultimate element analysis of SOFOUR-TEPE-Zn.

Elemental		N	C	H	S	O	N/S
%	Actual	10.22	48.16	3.90	6.05	15.74	1.69
(mass)	Theoretical	11.30	53.05	3.24	6.44	12.84	1.75

Table S5. Dual-site Langmuir parameter fits for C_2H_2, and the Single-site Langmuir parameter fits for CO_2 in SOFOUR-TEPE-Zn and SOFOUR-1-Zn.

		Site A			Site B		
		$\frac{q_{A,sat}}{\mathrm{mol/kg}}$	$\frac{b_{A0}}{\mathrm{Pa}^{-1}}$	$\frac{E_A}{\mathrm{kJ\ mol}^{-1}}$	$\frac{q_{B,sat}}{\mathrm{mol/kg}}$	$\frac{b_{B0}}{\mathrm{Pa}^{-1}}$	$\frac{E_B}{\mathrm{kJ\ mol}^{-1}}$
SOFOUR-TEPE-Zn	C_2H_2	2.95	2.454E-11	45.6	1.45	8.309E-10	25.3
	CO_2	1.8	1.433E-10	26.25			
SOFOUR-1-Zn	C_2H_2	2.3	2.170E-03	/	1.65	8.287E-06	/
	CO_2	4.4	4.580E-05				

Table S6. Comparison of the adsorption capacity and C_2H_2/CO_2 (50/50, v/v) selectivity and heat of adsorption data of SOFOUR-TEPE-Zn with other best-performing materials at 298 K and 1.0 bar.

Sample	**S_{BET} (m^2 g^{-1})**	**C_2H_2 (cm^3 g^{-1}) 0.1 bar/0.5 bar**	**C_2H_2 (cm^3 g^{-1}) 1.0 bar**	**CO_2 (cm^3 g^{-1}) 1.0 bar**	**$S_{C2H2/CO2}$ (50/50) 1.0 bar**	**Q_{st} (kJ mol^{-1}) C_2H_2**	**Ref.**
SOFOUR-TEPE-Zn	**459**	**72/82.69**	**89.04**	**14.06**	**16833**	**45.5**	**This work**
ZNU-1	**532**	**56.44/70**	**76.3**	**38.1**	**56.6**	**54.0**	**[19]**
BSF-4	**437**	**32.07/45.31**	**53.36**	**35.95**	**9.8**	**35.0**	**[19]**
HOF-FJU-1	**382.4**	**36/40.2**	**43.39**	**3.88**	**6675 (323 K)**	**46.73**	**[4]**
MIL-160	**1138**	**81.68/172.07**	**191.86**	**90**	**10.0**	**31.8**	**[20]**
CAU-10-H	**627**	**26.99/76.5**	**89.8**	**60**	**4.0**	**27.0**	**[21]**
CAU-10-NH_2	**403**	**57.79/76.34**	**80.06**	**46.55**	**10.8**	**31.3**	**[22]**
SIFSIX-Cu-TPA	**1272**	**111.9/**	**185.51**	**107.22**	**5.3**	**39.1**	**[23]**
ZJU-280	**257**	**66.63/94.9**	**105.28**	**71.01**	**18.1**	**50.6**	**[24]**
FJU-90a	**1572**	**58/154.5**	**180**	**103**	**4.3**	**25.1**	**[25]**
ATC-Cu	**600**	**86/107.52**	**112.22**	**90.04**	**53.6**	**79.1**	**[26]**
UTSA-74a	**830**	**34/88.9**	**107.97**	**67.9**	**9.0**	**31.0**	**[27]**
Zn-MOF-74	**996**	**14.8/124**	**150**	**146**	**2.8**	**24.7**	**[27]**
SOFOUR-1-Zn	**612**	**52/61**	**69**	**81**	**6.6**	**57.0**	**[28]**
SIFSIX-22-Zn	**641**	**83.27/111.61**	**127**	**95**	**6.5**	**36.5**	**[28]**

NCU-100	**358**	**24.64/97.44**	**102.37**	**11**	**1787.0**	**60.5**	**[29]**
NUS-71	**582**	**9.63/26.45**	**44.11**	**10.29**	**16.0**	**32.7**	**[30]**
CPL-1-NH$_2$	**103**	**35.39/40**	**41.2**	**4.7**	**119.0**	**50.0**	**[31]**
Cu^I@UiO-66 -(COOH)$_2$	**302**	**30.02/43.4**	**51.74**	**19.0**	**185.0**	**74.5**	**[32]**
SNNU-45	**1006**	**61.3/114.1**	**133.95**	**97**	**4.5**	**39.9**	**[33]**
TIFSIX-2-Cu-i	**685**	**66.97/83**	**91.84**	**96.3**	**10.7**	**46.3**	**[34]**
FeNi-M'MOF	**383**	**91.1/101.5**	**133**	**84**	**22.0**	**60.3**	**[35]**
ZJU-74a	**694**	**49/85.8**	**85.7**	**70.1**	**36.5**	**45.0**	**[36]**
NKMOF-1-Ni	**382**	**47.96/55.5**	**61**	**51.1**	**22.0**	**60.3**	**[37]**
HOF-3a	**165**	**24.04/4742.5**	**46.82**	**21**	**21.5**	**19.5**	**[38]**
DICRO-4-Ni-i	**398**	**23.72/36.3**	**43**	**23**	**13.9**	**37.7**	**[39]**
JCM-1	**550**	**39.79/63.5**	**76**	**38.1**	**13.7**	**36.9**	**[40]**
ZJU-50a	**1570**	**86.79/166.98**	**192**	**100**	**12.0**	**40.0**	**[41]**
FJU-6-TAPB	**1306**	**24.28/73**	**109.86**	**58**	**3.1**	**29.0**	**[42]**
UTSA-300	**311**	**-/52.6**	**68.99**	**4.1**	**860**	**57.6**	**[43]**
MUF-17	**211**	**62.9/82.1**	**112**	**56.2**	**6.0**	**49.5**	**[44]**

Table S7. Comparison table of C_2H_2 productivity and purity of SOFOUR-TEPE-Zn with other best-performing materials at 298 K and 1.0 bar at 100% C_2H_2 recovery.

Sample	**C_2H_2 Productivity (cm^3 g^{-1})**	**C_2H_2 Purity (%)**	**C_2H_2 Recovery (%)**
SOFOUR-TEPE-Zn	**75.71**	**99.33**	**100**
SOFOUR-1-Zn	**50.40**	**81.31**	**100**
HOF-FJU-1	**37.63**	**95.63**	**100**
MIL-160	**133.50**	**88.47**	**100**
CAU-10-H	**51.52**	**69.34**	**100**
CAU-10-NH_2	**75.26**	**89.82**	**100**
SIFSIX-Cu-TPA	**121.86**	**80.11**	**100**
ZJU-280	**79.07**	**90.06**	**100**
FJU-90a	**116.26**	**79.62**	**100**
ATC-Cu	**74.37**	**95.12**	**100**
UTSA-74	**73.47**	**66.19**	**100**
ZNU-1	**63.39**	**97.80**	**100**
BSF-4	**38.30**	**89.34**	**100**

Table S8. Comparison table of the C_2H_2 productivity and recovery of SOFOUR-TEPE-Zn with other best-performing materials at 298 K and 1.0 bar for obtaining 99+% and 99.5+% C_2H_2 purity. (Blue represents the highest purity that can be achieved and the corresponding productivity and recovery)

Sample	C_2H_2 Purity of 99+%				C_2H_2 Purity of 99.5+%			
	Start tau of collection	C_2H_2 Purity (%)	C_2H_2 Productivity (cm^3 g^{-1})	C_2H_2 Recovery (%)	Start tau of collection	C_2H_2 Purity (%)	C_2H_2 Productivity (cm^3 g^{-1})	C_2H_2 Recovery (%)
SOFOUR-TEPE-Zn	~0	99.34	75.71	99.99	0.65	99.51	75.49	99.82
SOFOUR-1-Zn	227.19	99.22	36.96	73.02	291.67	99.50	35.84	70.97
HOF-FJU-1	5.52	99.02	36.29	96.39	6.44	99.52	36.06	95.81
MIL-160	103.44	99.03	109.98	82.34	123.85	99.51	106.40	79.61
CAU-10-H	167.44	99.00	20.16	39.30	180.78	99.50	18.82	36.39
CAU-10-NH_2	59.75	99.05	64.51	85.72	71.35	99.51	63.17	83.91
SIFSIX-Cu-TPA	431.47	95.21	64.51	52.88	/			
ZJU-280	54.26	99.05	66.98	84.78	133.09	99.43	55.55	70.28
FJU-90a	96.21	99.06	83.10	71.38	103.46	99.53	81.09	69.73
ATC-Cu	43.07	98.45	66.75	89.81	/			
UTSA-74	311.73	99.07	19.71	26.96	332.44	99.52	17.70	24.18
ZNU-1	2.98	99.00	62.72	98.75	4.23	99.51	62.27	98.22
BSF-4	20.34	99.02	33.38	87.20	24.08	99.51	32.70	85.45

References:

[1] R. Krishna, *RSC Advances* **2017**, *7*, 35724.

[2] R. Krishna, *ACS Omega* **2020**, *5*, 16987.

[3] A. L. Myers, J. M. Prausnitz, *AIChE Journal* **1965**, *11*, 121.

[4] Y. Yang, H. Zhang, Z. Yuan, J. Q. Wang, F. Xiang, L. Chen, F. Wei, S. Xiang, B. Chen, Z. Zhang, *Angew Chem Int Ed Engl* **2022**, e202207579.

[5] R. Krishna, *Microporous and Mesoporous Materials* **2014**, *185,* 30.

[6] R. Krishna, *RSC Advances* **2015**, *5*, 52269.

[7] R. Krishna, *Separation and Purification Technology* **2018**, *194*, 281.

[8] R. Krishna, *ACS Omega* **2020**, *5*, 16987−17004.

[9] D. Luo, C. Li, Y. Zhang, Q. Ma, C. Ma, Y. Nie, M. Li, X. Weng, R. Huang, Y. Zhao, L. Shui, X. Wang, Z. Chen, *Adv Mater* **2022**, *34*, e2105541.

[10] N. Chen, Y. Zhou, S. Cao, R. Wang, W. Jiao, *Green Energy & Environment* **2021**.

[11] Y. Wu, G. Xu, W. Zhang, C. Song, L. Wang, X. Fang, L. Xu, S. Han, J. Cui, L. Gan, *Carbohydr Polym* **2021**, *267*, 118166.

[12] V. I. Nefedov, M. N. Firsov, I. S. Shaplygin, *Journal of Electron Spectroscopy and Related Phenomena* **1982**, *26*, 65.

[13] X. Guo, Z. Zhang, J. Li, N. Luo, G.-L. Chai, T. S. Miller, F. Lai, P. Shearing, D. J. L. Brett, D. Han, Z. Weng, G. He, I. P. Parkin, *ACS Energy Letters* **2021**, *6*, 395.

[14] D. Luo, C. Li, Y. Zhang, Q. Ma, C. Ma, Y. Nie, M. Li, X. Weng, R. Huang, Y. Zhao, L. Shui, X. Wang, Z. Chen, *Advanced Materials* **2022**, *34*, 2105541.

[15] G. Pan, J. Chen, K. Ge, L. Yang, F. Li, Z. Wang, S. Shi, X. Yang, Z. Zhou, A. Tang, W. Liu, Y. Sun, *Journal of Materials Chemistry C* **2019**, *7*, 4449.

[16] J. K. Saha, J. Podder, *Journal of Bangladesh Academy of Sciences* **2012**, *35*, 203.

[17] G. Nagaraju, Udayabhanu, Shivaraj, S. A. Prashanth, M. Shastri, K. V. Yathish, C. Anupama, D. Rangappa, *Materials Research Bulletin* **2017**, *94*, 54.

[18] Z. N. Kayani, M. Iqbal, S. Riaz, R. Zia, S. Naseem, *Materials Science-Poland* **2016**, *33*, 515.

[19] L. Wang, W. Sun, Y. Zhang, N. Xu, R. Krishna, J. Hu, Y. Jiang, Y. He, H. Xing, *Angew Chem Int Ed.* **2021**, *60*, 22865.

[20] Y. Ye, S. Xian, H. Cui, K. Tan, L. Gong, B. Liang, T. Pham, H. Pandey, R. Krishna, P. C. Lan, K. A. Forrest, B. Space, T. Thonhauser, J. Li, S. Ma, *J Am Chem Soc* **2022**, *144*, 1681.

[21] J. Pei, H. M. Wen, X. W. Gu, Q. L. Qian, Y. Yang, Y. Cui, B. Li, B. Chen, G. Qian, *Angew Chem Int Ed.* **2021**, *60*, 25068.

[22] X. Zhang, R.-B. Lin, H. Wu, Y. Huang, Y. Ye, J. Duan, W. Zhou, J.-R. Li, B. Chen, *Chemical Engineering Journal* **2022**, *431*.

[23] H. Li, C. Liu, C. Chen, Z. Di, D. Yuan, J. Pang, W. Wei, M. Wu, M. Hong, *Angew Chem Int Ed.* **2021**, *60*, 7547.

[24] Q.-L. Qian, X.-W. Gu, J. Pei, H.-M. Wen, H. Wu, W. Zhou, B. Li, G. Qian, *Journal of Materials Chemistry A* **2021**, *9*, 9248.

[25] Y. Ye, Z. Ma, R. B. Lin, R. Krishna, W. Zhou, Q. Lin, Z. Zhang, S. Xiang, B. Chen, *J Am Chem Soc* **2019**, *141*, 4130.

[26] Z. Niu, X. Cui, T. Pham, G. Verma, P. C. Lan, C. Shan, H. Xing, K. A. Forrest, S. Suepaul, B. Space, A. Nafady, A. M. Al-Enizi, S. Ma, *Angew Chem Int Ed.* **2021**, *60*, 5283.

[27] F. Luo, C. Yan, L. Dang, R. Krishna, W. Zhou, H. Wu, X. Dong, Y. Han, T. L. Hu, M. O'Keeffe, L. Wang, M. Luo, R. B. Lin, B. Chen, *J Am Chem Soc* **2016**, *138*, 5678.

[28] D. Sensharma, D. J. O'Hearn, A. Koochaki, A. A. Bezrukov, N. Kumar, B. H. Wilson, M. Vandichel, M. J. Zaworotko, *Angew Chem Int Ed.* **2022**, *61*, e202116145.

[29] J. Wang, Y. Zhang, Y. Su, X. Liu, P. Zhang, R. B. Lin, S. Chen, Q. Deng, Z. Zeng, S. Deng, B. Chen, *Nat Commun* **2022**, *13*, 200.

[30] Z. Zhang, C. Kang, S. B. Peh, D. Shi, F. Yang, Q. Liu, D. Zhao, *J Am Chem Soc* **2022**, *144*, 14992.

[31] L. Yang, L. Yan, Y. Wang, Z. Liu, J. He, Q. Fu, D. Liu, X. Gu, P. Dai, L. Li, X. Zhao, *Angew Chem Int Ed.* **2021**, *60*, 4570.

[32] L. Zhang, K. Jiang, L. Yang, L. Li, E. Hu, L. Yang, K. Shao, H. Xing, Y. Cui, Y. Yang, B. Li, B. Chen, G. Qian, *Angew Chem Int Ed.* **2021**, *60*, 15995.

[33] Y. P. Li, Y. Wang, Y. Y. Xue, H. P. Li, Q. G. Zhai, S. N. Li, Y. C. Jiang, M. C. Hu, X. Bu, *Angew Chem Int Ed.* **2019**, *58*, 13590.

[34] K.-J. Chen, Hayley S. Scott, David G. Madden, T. Pham, A. Kumar, A. Bajpai, M. Lusi, Katherine A. Forrest, B. Space, John J. Perry, Michael J. Zaworotko, *Chem* **2016**, *1*, 753.

[35] J. Gao, X. Qian, R. B. Lin, R. Krishna, H. Wu, W. Zhou, B. Chen, *Angew Chem Int Ed.* **2020**, *59*, 4396.

[36] J. Pei, K. Shao, J. X. Wang, H. M. Wen, Y. Yang, Y. Cui, R. Krishna, B. Li, G. Qian, *Adv Mater* **2020**, *32*, e1908275.

[37] Y. L. Peng, T. Pham, P. Li, T. Wang, Y. Chen, K. J. Chen, K. A. Forrest, B. Space, P. Cheng, M. J. Zaworotko, Z. Zhang, *Angew Chem Int Ed.* **2018**, *57*, 10971.

[38] P. Li, Y. He, Y. Zhao, L. Weng, H. Wang, R. Krishna, H. Wu, W. Zhou, M. O'Keeffe, Y. Han, B. Chen, *Angew Chem Int Ed.* **2015**, *54,* 574.

[39] H. S. Scott, M. Shivanna, A. Bajpai, D. G. Madden, K. J. Chen, T. Pham, K. A. Forrest, A. Hogan, B. Space, J. J. Perry Iv, M. J. Zaworotko, *ACS Appl Mater Interfaces* **2017**, *9*, 33395.

[40] J. Lee, C. Y. Chuah, J. Kim, Y. Kim, N. Ko, Y. Seo, K. Kim, T. H. Bae, E. Lee, *Angew Chem Int Ed.* **2018**, *57*, 7869.

[41] K. Shao, H. M. Wen, C. C. Liang, X. Xiao, X. W. Gu, B. Chen, G. Qian, B. Li, *Angew Chem Int Ed.* **2022**, *61*, e202211523.

[42] L. Liu, Z. Yao, Y. Ye, Y. Yang, Q. Lin, Z. Zhang, M. O'Keeffe, S. Xiang, *J Am Chem Soc* **2020**, *142*, 9258.

[43] R. B. Lin, L. Li, H. Wu, H. Arman, B. Li, R. G. Lin, W. Zhou, B. Chen, *J Am Chem Soc* **2017**, *139*, 8022.

[44] O. T. Qazvini, R. Babarao, S. G. Telfer, *Chemistry of Materials* **2019**, *31*, 4919.